Lithospheric and upper mantle structure of the northeastern Tibetan Plateau

Han Yue,[1] Y. John Chen,[1] Eric Sandvol,[2] James Ni,[3] Thomas Hearn,[3] Shiyong Zhou,[1] Yongge Feng,[1] Zengxi Ge,[1] Andrea Trujillo,[3] Yanbin Wang,[1] Ge Jin,[1] Mingming Jiang,[1] Youcai Tang,[1] Xiaofeng Liang,[1] Songqiao Wei,[1] Haiyang Wang,[1] Wenyuan Fan,[1] and Zheng Liu[1]

[1]   We use receiver functions calculated for data collected by the INDEPTH-IV seismic array to image the three-dimensional geometry of the crustal and upper mantle velocity discontinuities beneath northeastern Tibet. Our results indicate an average crustal thickness of 65 to 70 km in northern Tibet. In addition, we observe a 20 km Moho offset beneath the northern margin of the Kunlun Mountains, a 10 km Moho offset across the Jinsha River Suture and gently northward dipping Moho beneath the Qaidam Basin. A region in the central Qiangtang Terrane with higher than normal crustal Vp/Vs ratio of ∼1.83 can be the result of the Eocene magmatic event. In the Qiangtang Terrane, we observe a significant lithospheric mantle discontinuity beneath the Bangong-Nujiang Suture at 80 km depth which dips ∼10° to the north, reaching ∼120 km depth. We interpret this feature as either a piece of Lhasa Terrane or remnant oceanic slab underthrust below northern Tibet. We detect a ∼20 km depression of the 660-km discontinuity in the mantle transition zone beneath the northern Lhasa Terrane in central Tibet, which suggests this phase transition has been influenced by a dense and/or cold oceanic slab. A modest ∼10 km depression of the 410-km discontinuity located beneath the northern Qiangtang Terrane may be the result of localized warm upwelling associated with small-scale convection induced by the penetration of the sinking Indian continental lithosphere into the transition zone beneath the central Tibetan Plateau.

1.   Introduction

[2]   The Tibetan Plateau, with a relatively uniform high elevation of ∼5 km, was formed as a result of the continental collision between the Indian and Eurasian plate beginning 50–55 Ma [e.g., *Argand*, 1924; *Powell and Conaghan*, 1973; *Molnar*, 1988]. The Tibetan Plateau is amalgamated from the Lhasa, Qiangtang, Songpan-Ganzi (SG) and Qaidam Terranes [e.g., *Yin and Harrison*, 2000]. From south to north, the Bangong-Nujiang Suture (BNS), Jinsha River Suture (JRS) and Kunlun Fault (KF) (Figure 1) separate these Terranes. The deformation and evolution of the Tibetan Plateau has generally been attributed to (1) the wholesale underthrusting of Indian continental lithosphere beneath southern Tibet [e.g., *Ni and Barazangi*, 1984; *Tilmann et al.*, 2003; *Nábělek et al.*, 2009], (2) the uniform thickening and shortening of Eurasian lithosphere [e.g., *Dewey and Burke*, 1973; *Houseman and England*, 1986; *England and Searle*, 1986] and (3) the eastward stepwise extrusion of the Eurasian lithosphere along major strike-slip faults [*Tapponnier et al.*, 1982].

[3]   Within the last two decades, international broadband seismic experiments have been deployed across the Tibetan Plateau to investigate the crustal and upper mantle structure, including the PASSCAL Tibet seismic experiment in 1991 and 1992, INDEPTH I-III, Namche-Barwa, Southeastern Tibet, Hi-CLIMB and Sino-French experiments [*Owens et al.*, 1993; *Brown et al.*, 1996; *Nelson et al.*, 1996; *Owens and Zandt*, 1997; *Kosarev et al.*, 1999; *Kind et al.* 2002; *Vergne et al.*, 2002; *Sol et al.*, 2007; *Li et al.*, 2008; *Nábělek et al.*, 2009]. The Moho depth was found to be ∼60–80 km beneath the high Plateau from different receiver function studies and S converted to PmP phases [*Kind et al.*, 2002; *Vergne et al.*, 2002; *Nábělek et al.*, 2009; *Owens and Zandt*, 1997; *Tseng et al.*, 2009]. These studies found that the Moho depth shallows to the north and N-S
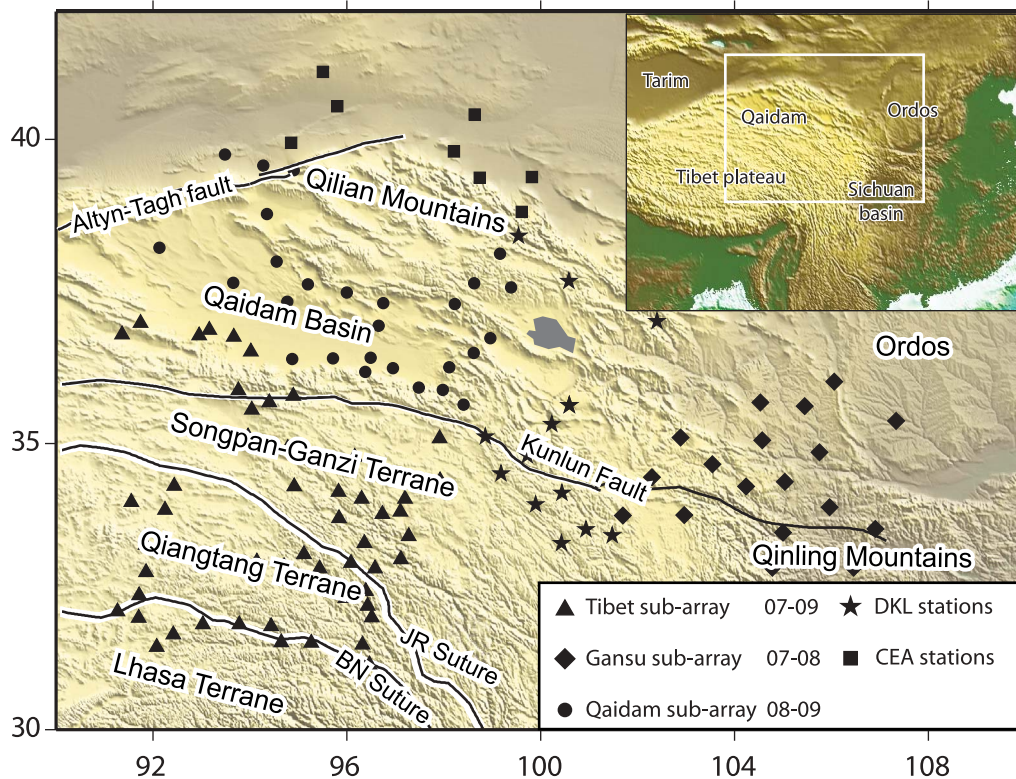
[1]Department of Geophysics, Peking University, Beijing, China.
[2]Department of Geological Sciences, University of Missouri, Columbia, Missouri, USA.
[3]Department of Physics, New Mexico State University, Las Cruces, New Mexico, USA.

Corresponding author: Y. J. Chen, Department of Geophysics, Peking University, Beijing 100871, China. (johnyc@pku.edu.cn)

Figure 1. Station locations of the I4 2-D array (triangles, diamonds and circles), DKL stations (stars) and China Earthquake Administration (CEA) stations (squares). The white rectangle in the top right of the map marks the position of the I4 array in the northeastern Tibetan Plateau. I4 stations in the south of the Kunlun fault (KF) were deployed for two years and those located to the north and east were deployed for one year. The DKL stations were deployed for one year. Only three months of CEA data were used. Also marked are the locations of the Altyn-Tagh Fault, Kunlun Fault (KF), Jinsha-River Suture (JRS), the Bangong-Nujiang Suture (BNS), the Songpan-Ganzi Terrane (SG), the Qiangtang Terrane and the Lhasa Terrane.

oriented linear receiver function profiles show step-like Moho offsets beneath the Jinsha River Suture and Kunlun Fault [e.g., *Zhu and Helmberger*, 1998; *Vergne et al.*, 2002; *Shi et al.*, 2009]. Moderate depressions of both the 410 km and 660 km discontinuities in northern Tibet were consistent with a low velocity upper mantle above the 410 km discontinuity [*Kosarev et al.*, 1999; *Kind et al.*, 2002]. S-wave receiver functions were used to image the base of the lithosphere across the Tibetan Plateau [e.g., *Kumar et al.*, 2006]. A discontinuity associated with a velocity decrease at a depth around 200 km was interpreted as the lithosphere-asthenosphere boundary (LAB) beneath southern Tibet and a similar velocity decrease is found ∼160 km deep beneath northern Tibet.

[4] Seismic tomography models indicate that upper-mantle velocity structure beneath the Tibetan Plateau is presently dominated by subduction of Indian continental lithosphere.

High velocity anomaly bodies were imaged through the whole upper mantle beneath the west segment of the collision front, which was interpreted as the subducted Tethys lithosphere [*Replumaz et al.*, 2004]. In central Tibet, along the Qingzang highway, a high velocity anomaly was found near 31° N, 89° E, beneath the Bangong-Nujiang Suture (BNS). This anomaly extends from 100 km to beneath 400 km depth [e.g., *Tilmann et al.*, 2003; *Li et al.*, 2008]. This high velocity body was interpreted as either the Indian continental lithosphere that thrusted beneath the Lhasa block and then subducted vertically into the upper mantle beneath the BNS [*Tilmann et al.*, 2003], or a high-angle (30°) subducting Indian continental lithosphere, which starts at the Himalayas and penetrates into the upper mantle transition zone beneath the central Tibetan Plateau [*Li et al.*, 2008]. In a separate study, a ∼350 km wide low velocity body was found 150 km beneath the Qiangtang Terrane near 34.5°N,

Table 1. Station Information of the Ascent and DKL Arrays

Array Name	Deployment Region	Instruments	Bandpass (s)	Station Number	Record Time
Tibet sub-array	SG and Qiangtang block	Guralp CMG-3 T, STS-2	0.02–120	57	2007.5–2009.9
Gansu sub-array	Eastern Tibet, Qinling and Ordos block	Mostly STS-2	0.02–120	18	2007.8–2008.8
Qaidam sub-array	Qaidam basin and Qilian mountains	Mostly STS-2	0.02–120	18	2008.8–2009.9
DKL array	Eastern Tibet	Guralp CMG-3ESP	0.02–30	12	2008.10–2009.8
CEA permanent stations	Northern to Qilian mountains	–	0.03–50	7	2008.10–2008.12
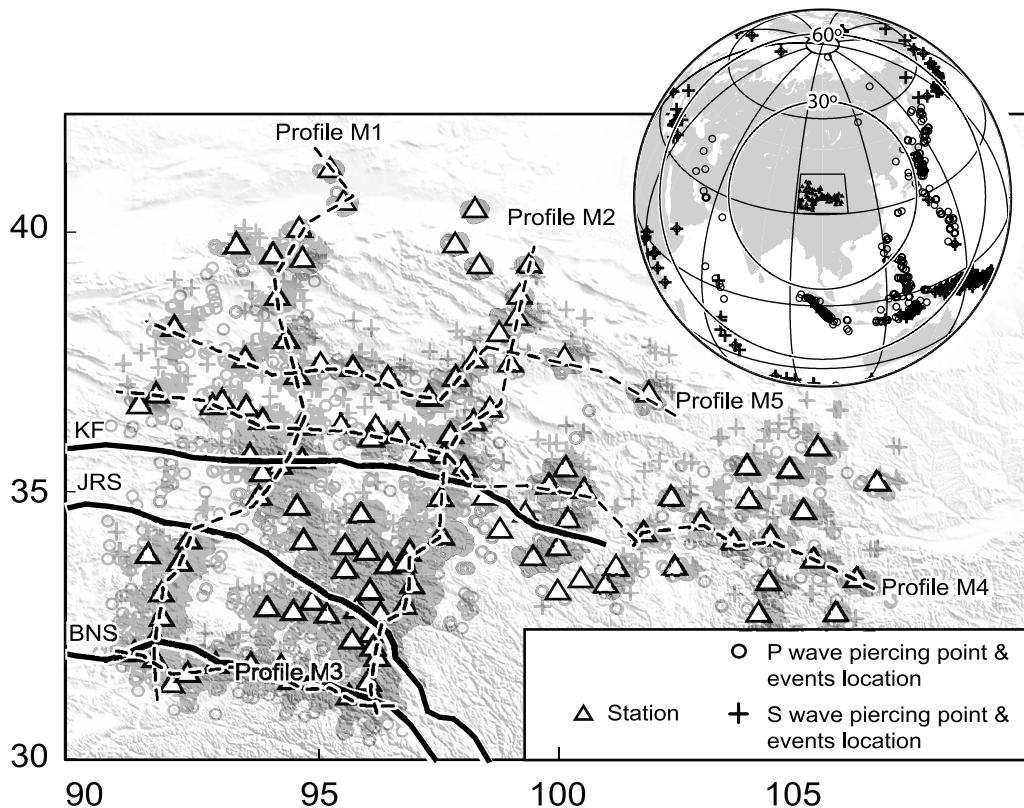
Figure 2. A map view of station locations (triangles). Ps and Sp converted-wave piercing points are denoted by circle and plus symbols, respectively. Locations of five seismic profiles (dashed lines) are also plotted on this map. The global map on the top right shows locations of the events used for calculating P wave receiver functions (circles) and S-wave receiver functions (plus symbols). The black frame marks the region of I4 deployment.

92°E [*Wittlinger et al.*, 1996]. This region was also found to have low Pn velocity, inefficient high frequency Sn propagation, low Q value, and a low Rayleigh wave phase velocity, all of which suggest a hot environment throughout the crust and upper mantle [*Ni and Barazangi*, 1983; *McNamara et al.*, 1995; *Liang and Song*, 2006; *Yang et al.*, 2010; *Bao et al.*, 2011]. These observations have been attributed to subduction-induced upwelling in the upper mantle beneath the Qiangtang and Songpan-Ganzi Terranes [*Tilmann et al.*, 2003].

[5] Our study region also covers the Qilian Mountains, the Qinling Mountains, the Qaidam Basin and the eastern part of the Qiangtang and Songpan–Ganzi Terranes (Figure 1). Intensive field observations indicate that this area has several large active strike-slip faults, including the Kunlun Fault (KF) and the Altyn-Tagh Fault [e.g., *Tapponnier and Molnar*, 1977; *Washburn et al.*, 2001; *Cowgill et al.*, 2009] (Figure 1). The Qilian Mountains have been rising at a rate of ∼0.5 mm/yr in the last 10 Myr [e.g., *Zheng et al.*, 2010]. Rapid uplifting and shortening is concentrated across several active faults at a rate of ∼3 mm/yr in the last 30,000 years [*Champagnac et al.*, 2010; *Chen et al.*, 2000]. Global Positioning System (GPS) measurements show the ground deformation pattern of the Qaidam and Qilian regions was produced by dislocations between blocks along large fault zones, which is distinct from the distributed glacier-like flow deformation of the elevated plateau [*Shen et al.*, 2003; *Gan*

et al., 2007]. Industry reflection profiles show that underthrusting and foreland wedge structures dominate the northern margins of Qaidam Basin [*Yin et al.*, 2007, 2008a, 2008b], but it is not clear if there is lithospheric thrusting of southern Qaidam lithosphere beneath the Kunlun Mountains. Qaidam Basin and Qilian Mountains may represent the early stage of the high-plateau formation (i.e., northward growth of the Tibetan Plateau) but lithospheric structures beneath the region are not well imaged to elucidate the deep deformation process. In this paper we use broadband seismic data from the INDEPTH-IV experiment to constrain three-dimensional lithospheric structure using receiver function methods. The study images the Moho across the region, as well as many upper mantle discontinuities.

2. Data and Methods

[6] The data used in this study were primarily collected as a part of the INDEPTH-IV (I4) experiment (Figure 1). The 2-D array was deployed in northeastern Tibet from May 30, 2007 to September 6, 2009 with the objective of studying the crust and upper mantle structure throughout the northeastern Tibetan Plateau. The geographic area covered by the array includes the central and eastern Qiangtang Terrane, Songpan-Ganzi Terrane, the entire Qaidam Basin and the Qilian Mountains (Figure 1). The stations are grouped into three sub-arrays: the Tibet sub-array, the Gansu sub-array
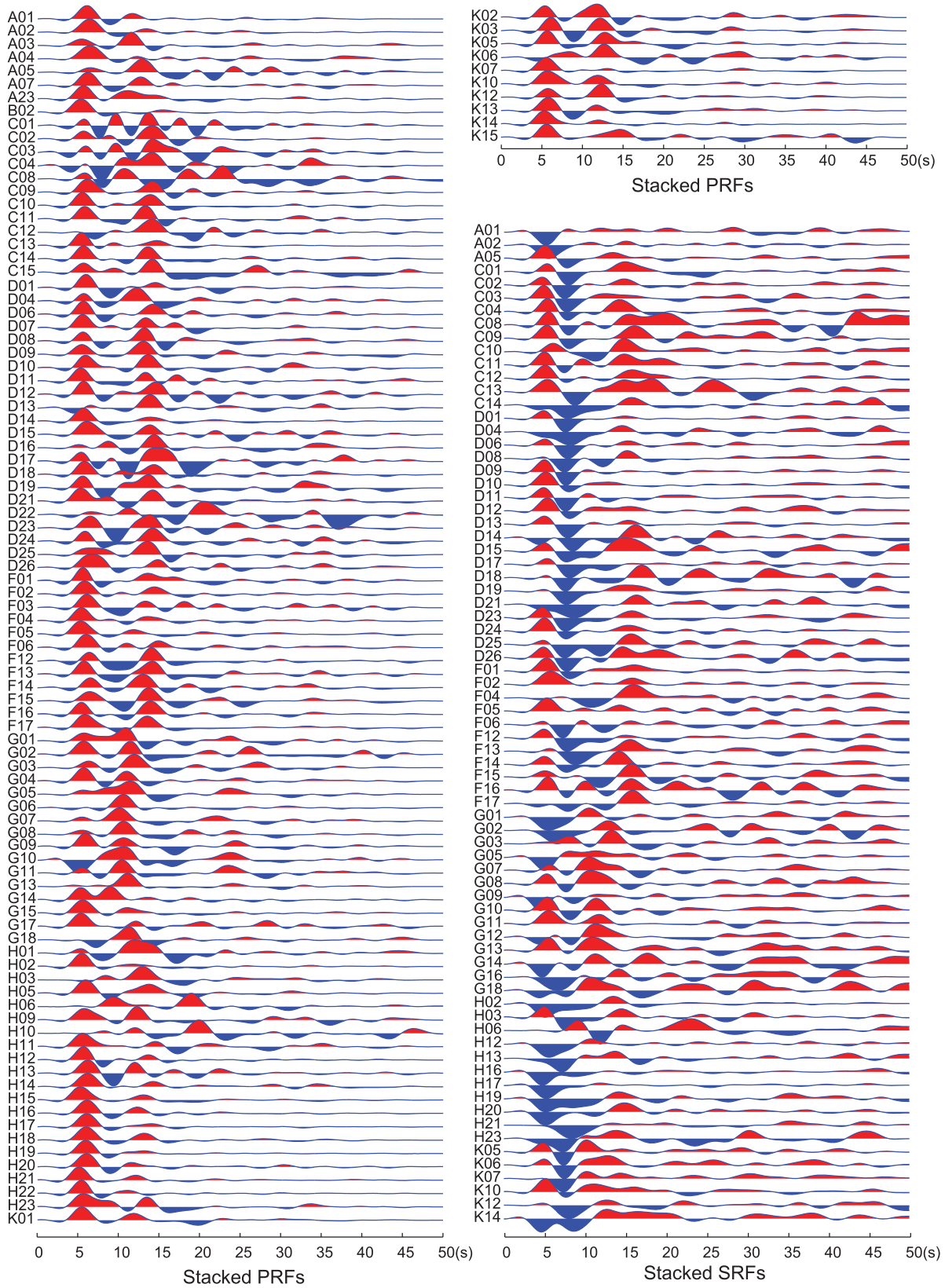
Figure 3a. Stacked P wave and S-wave receiver functions in time domain for each station. Station names are labeled on the left for each receiver function.
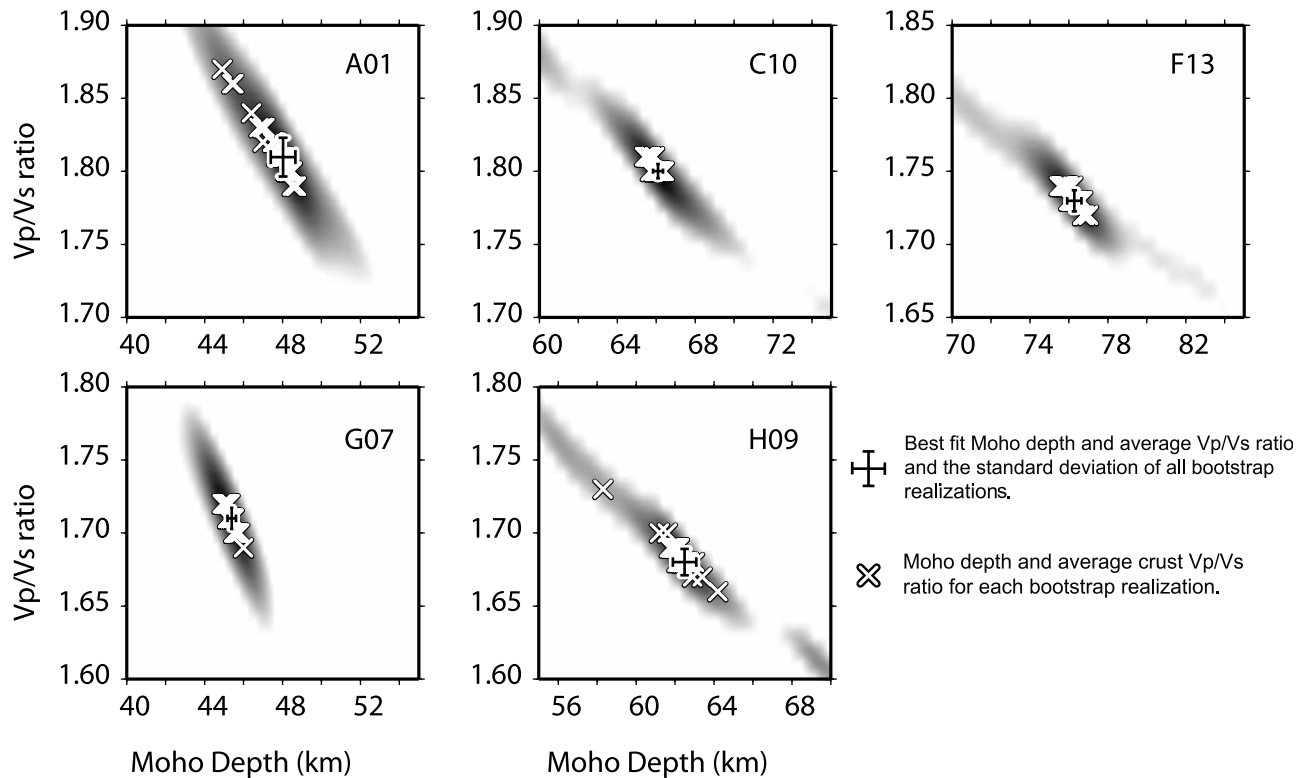
Figure 3b. P wave receiver function slant-stack results for 5 stations with the optimal result and standard deviation indicated by an error bar. Error analysis was done using 100 bootstrap realizations. Individual iterations marked by a white cross symbol.

and the Qaidam sub-array. The Tibet and Gansu sub-arrays are separated by 400 km. Peking University deployed 12 stations (DKL array in Figure 1) along the Kunlun Fault from September 2008 to August 2009 to fill in the gap between the I4 sub-arrays. The I4 array consisted of 93 portable three-component broadband seismic stations. The large Tibet sub-array, consisting of 57 stations, was deployed for approximately two years. The Gansu sub-array, consisting of 18 stations, was deployed in the Qinling Mountains between the Sichuan Basin and the Ordos block during the first year of this experiment. These instruments were re-deployed in the Qaidam Basin and Qilian Mountains in the following year, as the Qaidam sub-array (Figure 1). The I4 array stations were equipped with 5 Guralp CMG3-ESP sensors with a flat velocity response between 30 s to 0.02 s, 46 Streckeisen STS-2 sensors and 44 Guralp CMG-3 T sensors both with a flat velocity response between 120 s to 0.02 s. All I4 stations used the RefTek 130 data acquisition system at a sample rate of 25 samples-per-second (sps). DKL stations used Guralp CMG3-ESP sensors and RefTek 72A data acquisition systems at a sample rate of 40 sps. Seven China Earthquake Administration (CEA) broadband stations in Gansu Province were also used in this study. These instruments have a flat velocity response band from 50 s to 0.03 s. The station information is summarized in Table 1.

### 2.1. Receiver Function Processing and Stacking

[7] Receiver functions provide an important tool for imaging major discontinuities within the Earth from teleseismic

body waves [*Langston*, 1979]. The P wave receiver function (PRF) is obtained by deconvolving the vertical waveform from the radial waveform. Doing so removes the source time function and all P wave arrivals leaving just the train of P-to-S conversions. S-wave receiver functions (SRF) deconvolve the S-wave radial waveform from the vertical waveform thereby leaving only S-to-P conversions [e.g., *Farra and Vinnik*, 2000; *Vinnik and Farra*, 2002]. To the extent that the structure is flat-layered, the PRF will be consistent for different azimuths. Deconvolution of the tangential component of the P wave can help to resolve dipping and anisotropic structures. Over the last decade, SRFs have been widely used to image converted phases from the so-called lithosphere-asthenosphere boundary (LAB), for which the time interval of Ps conversions in PRFs is typically masked by multiple reflections [*Angus et al.*, 2006; *Wilson et al.*, 2006; *Yuan et al.*, 2006]. The relatively dense station spacing of the I4 array allows us to use Common Conversion Point (CCP) stacking or pre-stack migration techniques to image structures to their appropriate positions [*Yuan et al.*, 1997; *Bostock et al.*, 2001; *Wilson and Aster*, 2003].

[8] We selected ~10,600 P wave seismograms with high signal-to-noise ratio from 2633 teleseismic events with epicentral distances between 30° to 90° and mb >5.0 (Figure 2). A 75 s time window was used with each seismogram starting 10 s before the theoretical P wave arrival time. All raw data are pre-filtered with a two-pass fourth-order tapered cosine filter with a bandpass of 0.1–2.5 Hz. A time domain iterative deconvolution [*Ligorria and Ammon*, 1999] was applied to compute the receiver functions. A Gaussian filter with
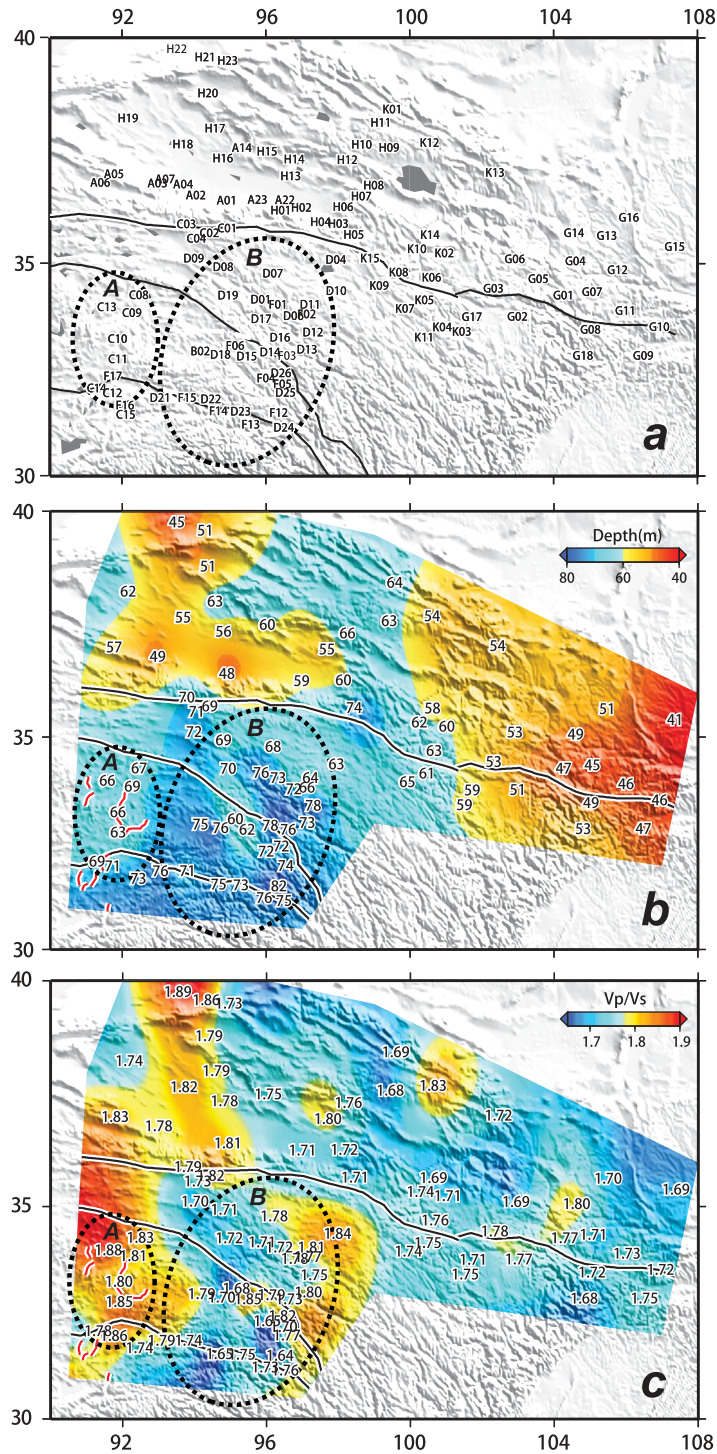
Figure 4. (a) Station names and locations. (b) Estimated crustal thickness. The numbers are the Moho depth beneath each station obtained by slant-stack algorithm. (c) Estimations of the averaged Vp/Vs ratios. The numbers are the average crustal Vp/Vs ratio beneath each station. The optimal results were selected considering the continuity of neighboring stations. The topography of Moho depth and Vp/Vs ratios was calculated by interpolating among these stations. The error analysis is summarized in Table S1 in the auxiliary material. Regions A and B are sorted by similar crustal properties. Region A is characterized by high Vp/Vs ratio (~1.83) and relatively thin crust (~67 km). Red lines are the normal faults in this area [*Styron et al.*, 2010]. Region B is characterized by a normal Vp/Vs ratio (~1.75) and thicker crust (70–75 km).
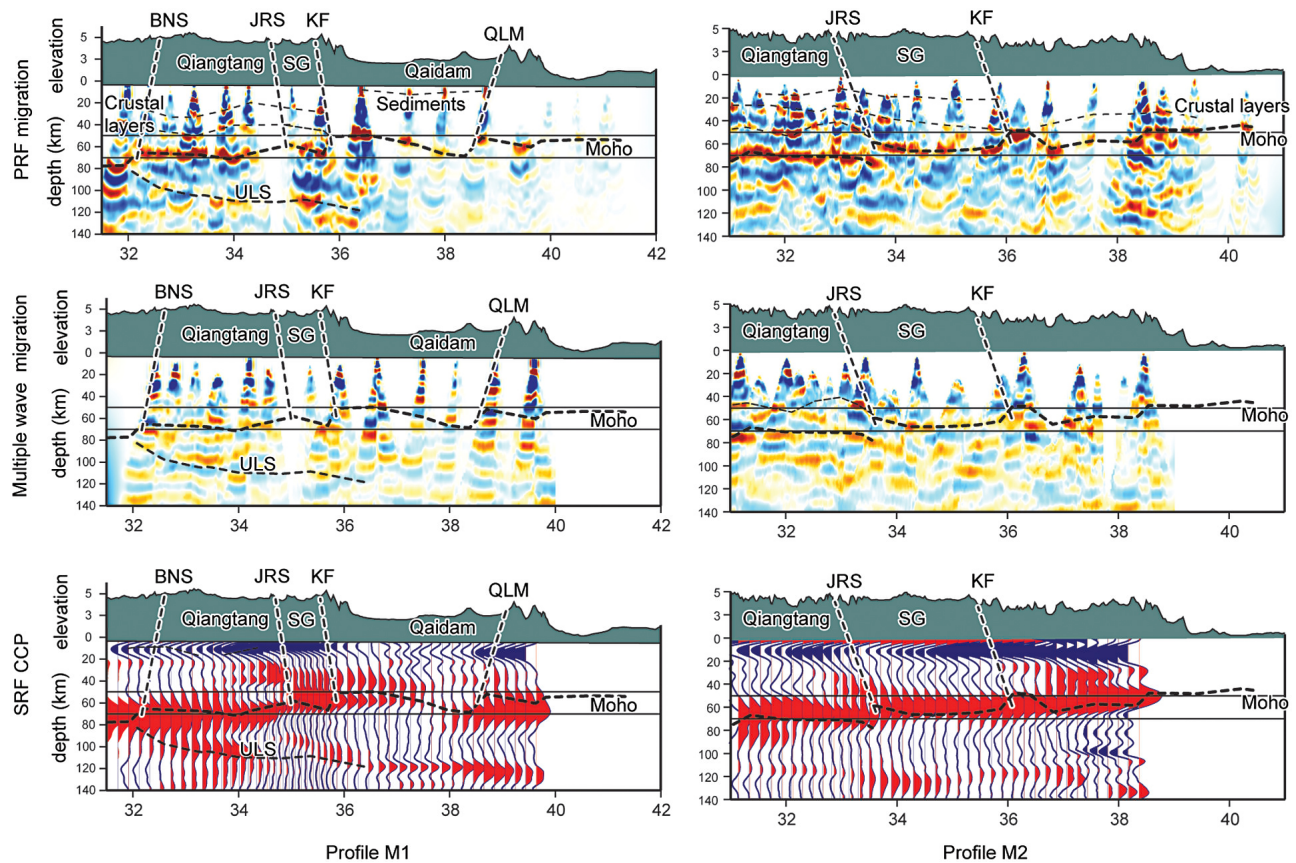
Figure 5. Migrated PRF images and common conversion point (CCP) stacks for profiles M1 and M2 (Figure 2). (top) P wave receiver function (PRF) migration images, (middle) multiple mode migration images, and (bottom) S-wave receiver function CCP stacking images. Thick dashed lines identify the Moho and the light dashed lines identify the underthrust Lhasa Terrane lithosphere slab (ULS) and the crustal layers. These lines were taken from the P wave migration image and plotted on the other images for comparison.

corner frequency of 2.5 Hz was applied to the deconvolved traces. In the classical PRF calculation, the vertical and radial amplitude ratios are used to estimate the incident P wave and converted S waves. This is an acceptable approach when the incident angle is small; however, this approach will introduce systematic phase variations into the receiver functions when the incident angle is large. We applied the free surface correction of *Kennett* [1991] to correct for this phase variation, which extracts the incident P and converted S waves from the vertical and radial component waveforms. For SRFs, we selected 1623 teleseismic S-wave records and 947 SKS waveform records from 723 events with mb ≥5.0. The epicentral distances of the selected events were 50° to 80° for S-waves and 90° to 110° for SKS-waves (Figure 2). The raw data was cut with a 60 s length time window, starting 40 s prior to the theoretical S wave arrival. The same bandpass filter was applied to the raw shear wave data, but with a lower corner frequency at 1 Hz. A lowpass Gaussian filter (1.5 Hz) was applied to the deconvolved traces. The RFs at each station were then stacked in the time domain and plotted in Figure 3a.

[9] Using the slant-stack method of *Zhu and Kanamori* [2000], the direct Ps converted phase and the multiply reflected phases were stacked in order to determine the optimal Moho depth and Vp/Vs ratio (Figure 3b). Assuming a horizontally stratified crustal layer, the arrival times of these converted waves are controlled by the Moho depth and compressional and shear wave velocities (Vp and Vs) beneath each station. In the slant-stack process, we assumed an average crustal Vp and performed a grid search of the optimal Vp/Vs ratio and crustal thickness values by maximizing the stacked energy of all the converted wave, including Ps, Ppps and Psps + Ppss phases. The average Vp for each station was interpolated from the Crust 2.0, a 3D global crustal velocity model developed by *Laske et al.* [2000]. To explore the validity of our reference model, we compared the average crustal P wave velocity of Crust 2.0 with the global model CUB 2.0 [*Ritzwoller et al.*, 2002], finding that the average crustal Vp difference is approximately 3% to 5%. The uncertainty of the slant-stack result is approximately proportional to the reference velocity model uncertainty. Assuming the velocity model uncertainty is 5%; the corresponding uncertainty due to the model inaccuracy is also 5%, which corresponds to 2.5 km for a 50 km thick crust. We used data from station A01 to test our error estimation and found changing the reference velocity by 5% Vp corresponds to a 3 km Moho depth variation and 0.02 Vp/Vs ratio variation. In our receiver
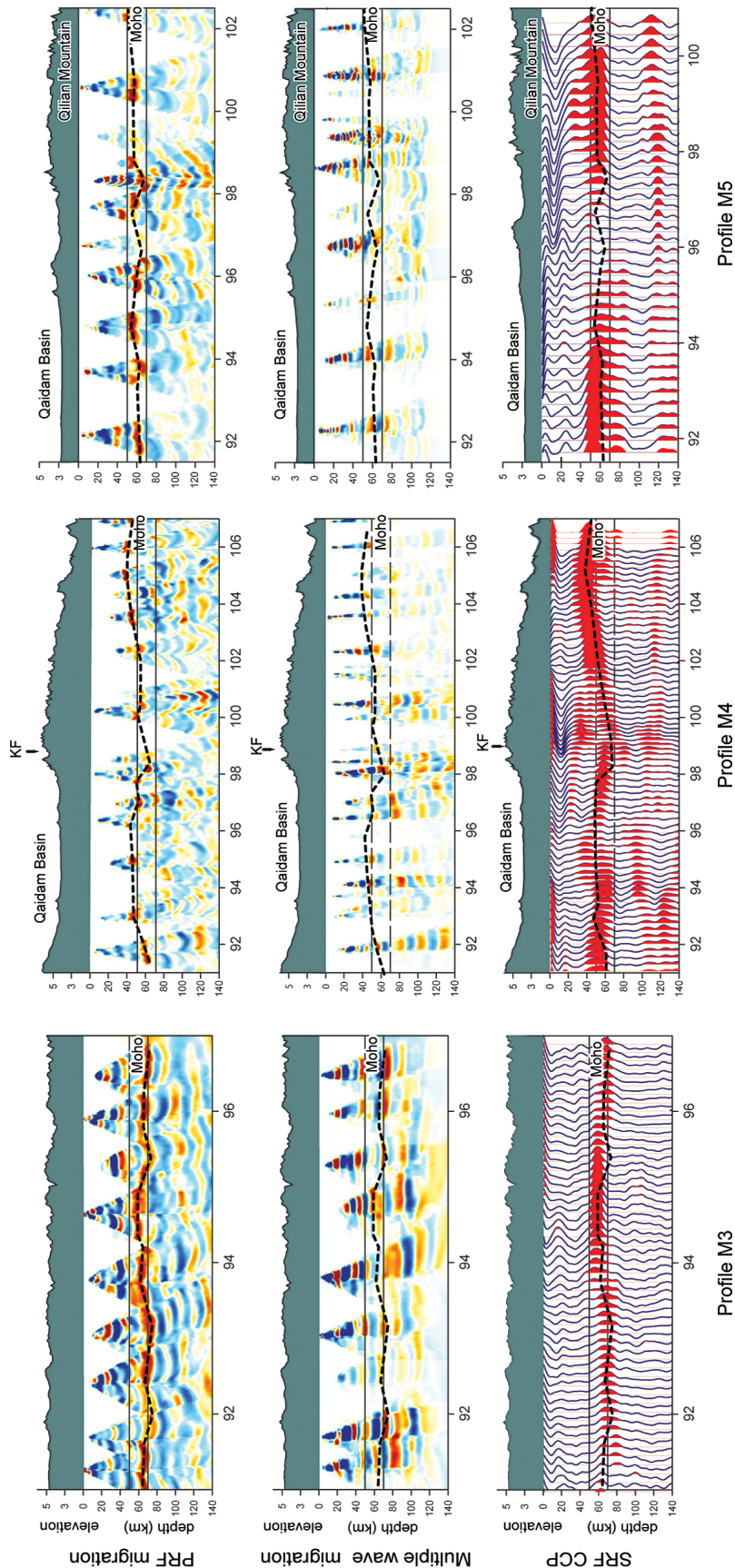
Figure 6. Migration images and CCP stack images of profiles M3, M4 and M5. Thick dashed lines highlight the Moho geometry in the P wave migration image, which is the same as in Figure 5.
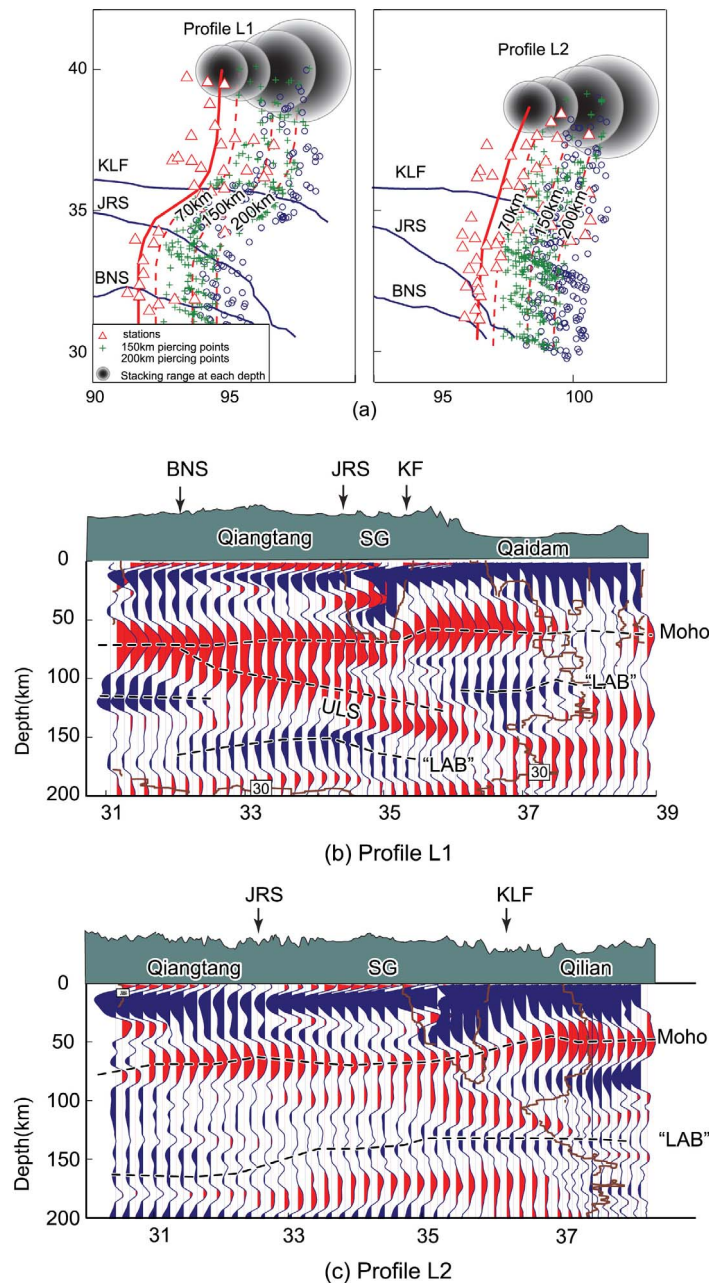
Figure 7. (a) Piercing points of S wave receiver functions at different depths. These piercing points were projected on two N-S trending, east-dipping profiles to maximize the amount of stacked data. Thick red solid lines show the profile location at the surface and the thin dashed red lines show the profile position at various depths. The black circles identify the range for Gaussian weight stacking at different depths. (b and c) SRF CCP stacking results for the profiles L1 and L2. The brown curved boundary delineates where more than 30 receiver functions were stacked and serve as a reliability indicator. The black dotted lines show the location of Moho, the top of the remnant oceanic slab or the underthrust Lhasa Terrane lithosphere slab (ULS), and the negative interface which may associate with the lithosphere-asthenosphere-boundary (LAB).

function calculations, the vertical resolution is mainly controlled by the applied low-pass Gaussian filter, which is ~5 km. From 100 slant-stack results (Table S1 in the auxiliary material), 81 stations (Table S2) had stable Moho depths and Vp/Vs ratio estimates (data quality and images are shown in Figure 3b, Table S1, and Figures S1–S5 in

Text S2).[1] Due to the noise levels and the instability inherent in the slant-stack method, we often observe multiple peaks, which can make our results ambiguous. Instead

---

of excluding the results for these stations, we chose those peaks that are consistent with the nearest-neighbor stations. We manually selected each consistent Moho depth and Vp/Vs ratio; then we interpolated these data to produce 2-D maps of both parameters (Figure 4). The standard deviations of Moho depth and Vp/Vs ratio for each station, obtained by 100 bootstrap realizations, are shown in Figure 3b and Table S1.

2.2. Receiver Function Migration and CCP Stacking

[10] In order to obtain a more detailed image of the Moho geometry and to detect any major lithospheric interfaces, we applied a regularized Kirchhoff migration approach. This migrates direct and multiply converted waves in order to move the signal to the actual conversion locations [*Dellinger et al.*, 2000; *Wilson and Aster*, 2003]. *Wilson and Aster* [2003] provided a method to migrate the PRFs of a linear seismic array using a 1D reference model. Our seismic array covered a large region, where the crustal structure appears to have significant heterogeneity, therefore, errors in any single 1D reference velocity model will lead to significant depth errors in migrated interfaces. For each station, we interpolated a 1D-velocity model from model CUB 2.0 and used that local 1D-velocity model in the Kirchhoff migration of the station's PRFs, and then stacked the migrated signals from different stations. The relatively low-resolution (2 × 2 degree) global velocity model cannot provide an optimal local velocity model; however, it is the best resolution model available for this analysis. The CUB 2.0 model includes, for example, abrupt velocity contrasts across the KF. For other regions, we do not observe strong velocity heterogeneities and thus it is reasonable to use linear interpolation; a more accurate model probably would not produce significant changes in our migrated RF image [*Chen et al.*, 2006]. Our RF images are also corrected for elevation. We consider five profiles along the portion of the I4 array with the most dense station coverage region: two N-S profiles and three E-W profiles (Figure 2). Ps conversion and multiple conversions (Ppps) were migrated for all five 2D profiles (Figures 5 and 6).

[11] We applied the CCP stacking technique [*Dueker and Sheehan*, 1997; *Wittlinger et al.*, 2004; *Shi et al.*, 2009] to the SRFs for comparison with the PRF migration images. The migration approach obtains detailed interface geometry where ray density is high. However, lacking dense ray coverage, as is the case for our SRF database, migration smears the waveforms along isochrons, which causes the interface images to be irregular. Assuming a horizontally layered medium, the CCP stacking approach involves tracing each raypath, back-projecting the waveforms along the theoretical raypath, and bin stacking the waveforms to estimate the average interface depth. CCP stacking is not sensitive to small-scale interface variations and will produce an intrinsically smooth image. For traditional PRF ray-tracing schemes, a plane wave assumption is applied to trace the theoretical raypath, in which the incident P wave and Ps conversions are assumed to have the same ray parameter. However, the plane wave assumption is not valid for SRF ray tracing: tracing the Sp phases with the S wave ray parameter will cause a piercing point location-error that increases with depth. This effect may produce ∼40 km

piercing point location-error when raytracing a 200 km deep Sp conversion. To avoid this error, we calculated the theoretical ray parameters of Sp phases converted at different depths for each source-converter-receiver set and used correct raypaths for each Sp conversion to obtain the piercing points at different depths. Then we generated evenly distributed bins along designated profiles. For each bin, the SRFs with piercing points in the bin were stacked using a Gaussian-weighting scheme. Because the SRF rays spread over a greater area with increasing depth, we increase the size of the stacking bins with depth in order to maintain a consistent SRF piercing point number (Figure 7). More details about the stacking technique are discussed in the auxiliary material. The same profiles were used to stack the SRFs and the PRFs to facilitate comparison and the results are shown in Figures 5 and 6.

[12] In order to image the uppermost mantle using SRFs, we excluded deep earthquakes at certain epicentral distances (75–95 degrees), for which the Sp phase may be contaminated by multiple P wave surface reflections, such as the pPP, pPPP and pPPPP, and can mask the upper mantle conversions in our SRFs [*Wilson et al.*, 2006; *Yuan et al.*, 2006]. SKS waves, which produce several artificial discontinuities, are also excluded. We generated two east dipping N-S strike profiles (Figure 7) from stacked SRFs.

[13] P waves from an epicentral distance greater than 30° penetrate into the mantle transition zone and are sensitive to the topography of the 410-km and 660-km discontinuities (Figure 8). Both Kirchhoff migration and CCP methods were applied to the PRFs and yielded similar results. The CCP method was preferred because it was more amenable to make a 3D surface. We stacked the PRFs on a 60 × 60 km grid with lateral increments of 30 km, and measured the depths of the 410-km and 660-km conversions from each CCP stack. The thickness of the mantle transition zone was calculated by differencing these two depth estimates (Figure 8).

3. Results and Discussion

3.1. Crustal Structure

[14] The Moho topography interpolated from the slant-stack result (Figure 4b) yields a picture of the crustal structure of the northeastern Tibetan Plateau. An average crustal thickness of about 70 km was found beneath the high plateau. The high plateau can be grouped into two regions: The central part of the Qiangtang Terrane (region A) is characterized by a thick crust (∼67 km) with a high Vp/Vs ratio of ∼1.83 (Region A in Figure 4). The eastern part of the Qiangtang and Songpan-Ganzi Terranes (region B in Figure 4), is characterized by a thicker crust (∼73 km) and relatively low Vp/Vs ratio (∼1.75). These results are comparable to those of *Vergne et al.* [2002]. Since we are using the same method and study the same region, the slight difference in Vp/Vs ratios between these two studies is mostly due to the assumed average crustal P wave velocity. The velocity structure resolved by our slant-stack algorithm is in general agreement with the shear wave velocity model resolved by ambient noise surface wave tomography [*Fan et al.*, 2012]. Our average crustal shear wave velocity from slant stacking is 3.5 km/s and 3.7 km/s for region A and B, respectively, in contrast to 3.4 km/s and 3.47 km/s for these two regions in the ambient noise surface wave
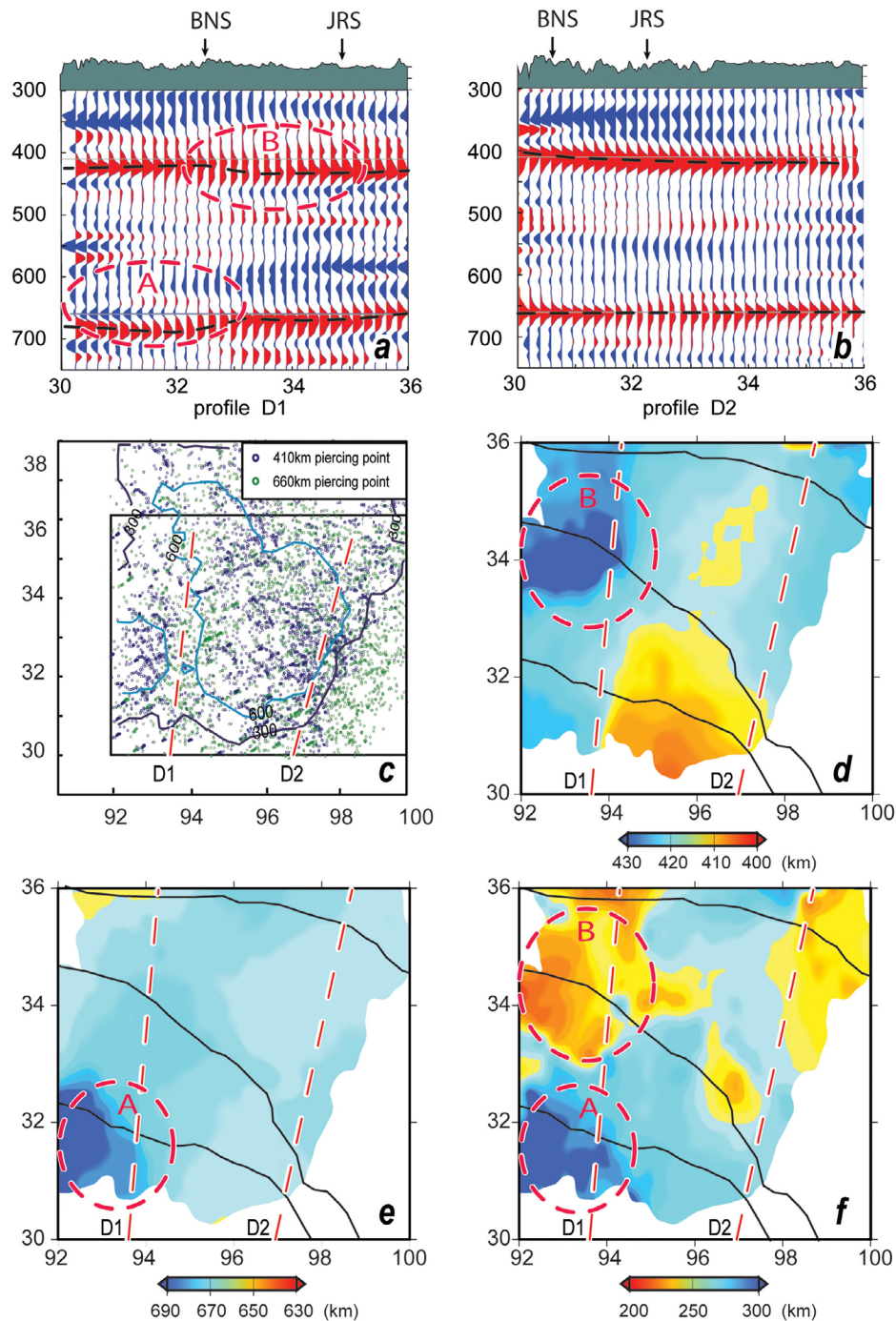
Figure 8. (a and b) P wave receiver function CCP image of the mantle transition zone of profiles D1 and D2 in Figure c. (c) Blue and green points representing piercing points of PRFs on 410-km and 660-km depths. Red dash lines represent the locations of profiles D1 and D2. Contours show the number of data stacked. (d and e) Topography of 410-km and 660-km discontinuity measured from P wave (CCP) respectively. Only the region with stacking numbers greater than 300 stacked waveforms is plotted. (f) Transition zone thickness obtained by subtraction the depth of 660-km interface from the depth of 410-km interface. Area A marks the depression of the 660-km discontinuity and area B marks the location of the depressed 410-km discontinuity.

tomography model of *Fan et al.* [2012] tomography model. Thus our crustal shear velocities are 3–7% higher than shear velocity in the tomography model. The particle motion of the Ps converted waves used in the PRF

calculation is nearly horizontal, in contrast to the vertical particle motion of the SV waves used by the ambient noise tomography. Therefore, the shear wave velocity differences between these two models may be partly attributed to the

shear wave radial anisotropy (with SV faster than SH) in central and eastern Tibet [*Shapiro et al.*, 2004]. The isotropic shear wave velocity model of *Fan et al.* [2012] indicates the lateral velocity contrast between the regions A and B are better defined in the upper crust (shallower than 40 km), but region A has a higher velocity gradient in the lower crust. This velocity structure is consistent with the crustal structure model reported by *Vergne et al.* [2002], in which the central Qiangtang Terrane is underlain by a mafic lower crust with relatively high Vp/Vs ratio greater than 1.8 [*Christensen*, 1996]. Region A in the Qiangtang Terrane is characterized by normal faults, hot springs, and widely distributed Eocene magmatic rocks [*Guo et al.*, 2006; *Roger et al.*, 2000]. These observations are probably related to the northward subducting Lhasa Terrane during the Miocene, (also discussed in the upper mantle structure section) [*Ding et al.*, 2003]. The slant stacking of PRFs indicates that the Qaidam Basin has relatively shallow Moho depth (50–55 km), with an abrupt depth change (from 70 to 50 km) across the northern margin of the Kunlun Mountains. In contrast, the Moho depth decreases gradually to the east as the elevation decreases, indicating that much of the topography is isostatically compensated. The high average crustal Vp/Vs ratio in the crust under the Qaidam Basin is probably related to a thick (~15 km) sediment layer [*Yin et al.*, 2008a].

[15] The first order crustal structural features resolved by the migration of the Ps conversions, migration of the P wave multiple reflections, and SRF CCP stacking are all similar (Figures 5 and 6). Within each of the major tectonic terranes that comprise the high Tibetan Plateau (>5 km), we observe an essentially flat Moho. Along profiles M1 and M2, Moho depth decreases in depth to the north: from 70 ~ 75 km depth in the Qiangtang Terrane to ~50 km depth in the Qaidam Basin. We observe Moho offsets at the major block boundaries: a ~10 km offset is found beneath the BNS (profile M1), a 10 km offset is found along the JRS (Profile M2), and ~20 km offset is found along the front of the Kunlun Mountains (Profile M1, M2 and M4). The Moho offset at the northern margin of the Kunlun Mountains was observed in previous studies [*Zhu and Helmberger*, 1998; *Vergne et al.*, 2002; *Shi et al.*, 2009]. *Karplus et al.* [2011] used wide-angle reflection seismic data of the I4 high resolution active-source seismic profile across the Kunlun Mountains to image the crustal structure. They observed a Moho depth offset (~18 km) and Moho overlap beneath the North Kunlun Thrust (between 36.4° N and 36.6° N). In their results, the Moho locates at 70 km depth to the south of KF and 52 km depth to the north of KF, which is generally consistent with the Moho depth found in this study (Figure 5). In our observations (profile M1 in Figure 5), the Moho offset occurs within the gap of station coverage beneath the northern margin of Kunlun Mountains, which is between 35.7° N and 36.2° N and is located at least ~50 km south of the offset in the study of *Karplus et al.* [2011]. Allowing for our lower resolution, our results are compatible with that higher resolution study.

[16] The Moho beneath the Qaidam Basin has a 5° dip toward the north from 50 km depth at 36° N to ~65 km depth at 38° N (Figure 5, profile M1). The same Moho depth variation is apparent in profile M4 and M5 (Figure 6). The Moho depth is ~50 km beneath the southern margin of the Qaidam Basin (profile M4) and 55–65 km deep beneath

the northern margin (profile M5), the offset of which is consistent with the image of profile M1. The observed Moho geometry indicates that the entire Qaidam Basin crust dips to the north. This northward dipping Moho may be related to the crustal thickening of the northern Qaidam and Qilian thrust-belt [*Yin et al.*, 2008a, 2008b], where the Qilian Mountains are probably partially overriding the Qaidam Basin. Assuming this to be the case, the weight of the Qilian Mountains would load the northern Qaidam margin, depressing the lithosphere. We also observe a prominent discontinuity at about ~15 km depth beneath the Qaidam Basin (Profile M1), which we interpret as the basement-sediment interface. Similar thicknesses of the sedimentary layer were also found in the western Qaidam basin from the active seismic reflection profiles [*Yin et al.*, 2008a].

[17] The east-west profile M3 (Figure 6) is located near the surface trace of the BNS. The Moho depth varies between 60 ~ 70 km along this profile. In general, crustal thickness correlates with the topography suggesting isostatic balance. The upward bending of the Moho occurs between 94.5° to 95.5° E, beneath the Qiangtang block. Profile M3 crossed the BNS in this segment, but the waveforms are contaminated by the scattering from BNS. Profile M4 extends from the Kunlun Mountains, through the Qaidam Basin and into the Qinling Mountains. Moho depth shallows gradually to the east, tracking the topography decrease.

[18] Some inconsistency between PRF migration images and SRF CCP stacking images is caused by differences in the processing methods. SRF images have smeared interfaces with respect to depth due to the low-pass Gaussian filter and the S-wave low frequency content. The low-pass Gaussian filter also produces broader and stronger sidelobes on the primary converted phase, which show up as strong negative amplitude features in the shallow crust (Figure 5–7). CCP stacking also smears the interface into a broader and weaker feature. This artifact is clearest when the interface has a sharp offset, as for the Moho offset beneath KF where CCP stacking images the offset as two overlapping interfaces; or when the interface is dipping slightly, as for the Moho beneath the Qaidam Basin, where the SRFs image a wider and weaker interface. We only have one year of data in the Qaidam Basin, which is not enough to yield a high resolution SRFs image. The PRF migration images are primarily of value for the crustal thickness analysis, while we use our SRF images primarily for inferring upper mantle structure in regions in those regions where we have sufficient data density. We do gain confidence from the fact that our SRF images compare quite well with the PRF images for crustal features.

3.2. Upper Mantle Structure

[19] Several upper mantle discontinuities are observed in the Ps phase and multiple wave migration images of the PRF and the SRF CCP profiles. A prominent north-dipping interface, located between 92° and 96° E, in the mantle beneath the eastern Qiangtang Terrane, is clearly imaged on profiles L1 (Figures 7 as well as Figure S6 in Text S2), as well as in PRF profile M1 (Figure 5). In profile L1, this feature begins just below the Moho, directly beneath the BNS at 80 km depth, and has a relatively constant dip (~10°) down to 120 km depth beneath the Kunlun Mountains (Figures 5 and 7). The E-W profiles of the SRF CCP

stacking image (Figure S6 in Text S2) demonstrate that this interface does not extend very far to the east. Since there are fewer piercing points in the central portion of the study area, the robustness of this interface is not well constrained there, and it is still uncertain how much to the east of 96°E this interface extends. Although several other intermittent interfaces are indicated in the PRF migration image, we suspect they may be caused primarily by crustal multiples since we did not observe the corresponding interfaces in the SRF image.

[20] *Kosarev et al.* [1999] and *Kind et al.* [2002] used P wave receiver functions to image the crustal and upper mantle structures beneath the Tibetan Plateau. They presented migrated receiver function profiles and found both north dipping discontinuities in the upper mantle beneath the Lhasa Terrane and south-dipping discontinuities in the uppermost mantle beneath northern Tibet. The north-dipping interface was interpreted as the top of underthrusting Indian lithosphere [*Kosarev et al.*, 1999; *Kind et al.*, 2002; *Tilmann et al.*, 2003; *Li et al.*, 2008]. The south-dipping interface was interpreted as the top of underthrusting Eurasian mantle lithosphere. However, we did not image a continuous south dipping interface beneath Qiangtang and Songpan-Ganzi Terranes in either the PRF or SRF images. The receiver function images show evidence for mid crustal interfaces within the crust of the Qiangtang and Songpan-Ganzi Terranes (Figure 5). These interfaces will most likely generate multiple reverberations affecting the time window of any uppermost mantle conversions. If the ray density is low, these artificial interfaces tend to suggest different segments of a continuous interface. Since the Sino-French and PASSCAL 1991–1992 experiments have a relatively large station gap (>100 km) to the north of BNS, the southward subducting Eurasian lithosphere interpreted by *Kosarev et al.* [1999] and *Kind et al.* [2002] might be an artifact of segmented multiple conversion boundaries. In contrast, our receiver functions are constructed with dense station coverage in northern Tibet, and the north dipping conversion boundary that we detect is a continuous feature that is seen in both PRF and SRF images (Figures 5 and 7).

[21] We propose that the dipping discontinuity beneath the Qiangtang Terrane represents the top of the underthrust Lhasa Terrane lithospheric slab (ULS). Alternatively, it could be remnant oceanic lithosphere that subducted along the Bangong-Nujiang Suture before the Lhasa-Qiangtang continental collision in the Jurassic (100 ∼ 130 Ma) [*Girardeau et al.*, 1984; *Guynn et al.*, 2006; *Kapp et al.*, 2007]. If assuming a continental subduction, it was presumably emplaced after the continental collision, and this feature is presumably younger than the continental collision age (100 Myr). Widely distributed Cenozoic volcanic rocks, dated to 30–50 Ma, may be related to the continental subduction after the collision between Lhasa and Qiangtang Terrane [*Ding et al.*, 2003; *Roger et al.*, 2000; *Yin and Harrison*, 2000]. In this model, the ULS geometry is similar to the ongoing Indian continental subduction, which starts right beneath the suture and subducts to the north [*Kosarev et al.*, 1999; *Kind et al.*, 2002; *Li et al.*, 2008]. The dip angle of ULS (∼10°) is shallower than the Indian continental subduction (∼30°) beneath central Tibet, which implies the ULS rebounded after the lower slab detached. The SRF signal strength of the dipping interface is ∼70% of

that for the Moho. Assuming the Vp/Vs ratio in the upper mantle is 1.79 ∼ 1.85, the corresponding S wave velocity increase would be about 4%-9%. Pn wave tomography using the I4 data set indicates that the uppermost mantle in this region has a 3–6% low velocity anomaly [*Wang et al.*, 2012]. Therefore, the dipping velocity contrast could be large due to both the high velocity of the subducting material and low velocity of the overlying uppermost mantle. For a subducted continental crust, the phase transformation from quartz to coesite at 90 km depth will cause subducted continental crust to show a positive ∼2% Vp and Vs anomaly relative to the ambient mantle [*Weaver et al.*, 1979; *Hacker and Abers*, 2004], comparable to that of a subducted oceanic slab.

[22] If assuming the ULS is a remnant oceanic slab, temperature anomaly should not contribute significantly to the velocity contrast as the subducted slab would have to have been confined to the upper mantle on the order of 100 Ma. The velocity contrast could instead be produced by the higher Mg content of the subducted oceanic slab [*Kosarev et al.*, 1999]. The main upper mantle phase transformation expected for a subducting oceanic lithosphere is the basalt/gabbro-eclogite transition [e.g., *Gubbins et al.*, 1994]. Although eclogite has a lower shear wave velocity than ambient mantle rocks at zero pressure [*Anderson*, 2007], the theoretical shear wave velocity of hot (800–1000°C) eclogite at depths between 100 and 200 km is 3–4% higher than for the ambient mantle peridotites [*Connolly and Kerrick*, 2002; *Hacker et al.*, 2003]. Subducted oceanic lithosphere consists mostly of harzburgite, which has seismic velocities close to those of eclogite at this depth [*Hacker et al.*, 2003]. A thick layer of high-density material such as eclogitized oceanic crust would segregate in a relatively short time (∼10 Ma) [*Vlaar et al.*, 1994]. However, numerical modeling suggest that a stratified subducting oceanic plate with an eclogitic upper crust underlain by a depleted harzburgite layer could remain in the upper mantle for longer than 100 Ma [*Arndt et al.*, 2009]. The shallow dip angle (6°–10°) of the ULS is similar to that of the shallow angle subduction of the Farallon plate when it underlay Western North America [*Bird*, 1988; *Currie and Beaumont*, 2011]. Simulations of Farallon plate subduction show that a young oceanic subducted slab could remain in the upper mantle for a relatively long time, >70 Ma. Therefore, the ULS interface may plausibly represent a remnant slab of what was young subducted oceanic lithosphere. A preserved fossil slab feature similar to what we have observed was also found in the Slave province, Canada [e.g., *Bostock*, 1998; *Asencio et al.*, 2003].

[23] In the S-wave receiver function images beneath the Qiangtang and Songpan-Ganzi Terranes, we observe a prominent negative polarity interface near 150 km depth (Figure 7). Seismic images with negative amplitudes observed at this depth are often interpreted as the lithosphere-asthenosphere boundary (LAB) [*Wilson et al.*, 2006; *Yuan et al.*, 2006]. This interface also shows an offset beneath the Kunlun Mountains, and shallows ∼50 km toward the north. In profile L2 this interface is not as well resolved as in the west (i.e., profile L1). The depth of this interface is generally consistent with a feature labeled LAB under NE Tibet reported by *Kumar et al.* [2006]; however, our images show significant N-S variations in depth. If this

boundary is the LAB, then the lithosphere beneath the Qiangtang and Songpan-Ganzi Terranes would appear to be thickened by the underthrust Lhasa Terrane by 50–70 km.

3.3. Mantle Transition Zone

[24] The 410-km and 660-km velocity discontinuities of the mantle transition zone are well imaged beneath the I4 array (Figure 8). These discontinuities are interpreted as primarily the result of mineralogical phase changes in the olivine component within the mantle and the depth at which they occur is strongly sensitive on temperature. The 410-km and 660-km discontinuities have opposite slopes of their respective Clapeyron curve, which would require a 100°C temperature change for each 10 km change in transition zone thickness [*Helffrich*, 2000]. A cooled mantle associated with a subducted slab that extends across the transition zone will cause a thicker transition zone (elevated 410-km discontinuity and depressed 660-km discontinuity), while upwelling hot material will cause a thinner transition zone (depressed 410-km discontinuity and elevated 660-km discontinuity) [e.g., *Turcotte and Schubert*, 2002; *Thomas and Billen*, 2009]. Global transition zone topography shows expected transition zone thickening within subduction zones [*Deuss*, 2009; *Shearer*, 2000; *Hirose*, 2002; *Gu et al.*, 2003; *Lawrence and Shearer*, 2008], and thinning at several hot spot regions [e.g., *Fee and Dueker*, 2004]. The thickest mantle transition zone (>277 km) is observed beneath the southwest Pacific subduction zone, and the thinnest mantle transition zone (<212 km) is observed beneath Africa. [*Lawrence and Shearer*, 2008]

[25] Figure 8 shows the topography of the 410-km and 660-km discontinuities, and the thickness of the transition zone beneath northeastern Tibet. Only those regions with greater than 300 stacked piercing points are shown in this figure. Two cross-sections oriented N-S are shown in Figure 8 to highlight the locations of the elevated and depressed discontinuities, and the associated topography (Figure 8). For profile D1, the minimum depths of both 410-km and 660-km interfaces are shifted ~10 km deeper than global reference depths. A similar observation was previously made from receiver function studies in central Tibet [*Kosarev et al.*, 1999; *Kind et al.*, 2002]. This depression may be caused by inaccuracy in the reference velocity models of the upper mantle: generally, when the reference model has a higher velocity, the apparent interface depth will be greater than the real depth. Removing this systematic shift of both interfaces, we find the 410-km interface is depressed by 10 km near 34°N and the 660-km interface is depressed by 20 km near 32°N.

[26] The deep portion of the mantle transition zone velocity structure under central Tibet, constructed by triplication waveform modeling [*Chen and Tseng*, 2007; *Tseng and Chen*, 2008], has a relatively high Vp and ordinary versus This high velocity anomaly was interpreted as a remnant of hydrous subducted continental lithosphere. Considering the reference model inaccuracy, a 3% Vp change in the deep transition zone, as reported by *Chen and Tseng* [2007], will influence the interface depth by less than 3 km. Therefore, the apparent 20 km deflection of the 660-km interface cannot be caused by this velocity anomaly near the bottom of the transition zone. The 20 km depression of the 660-km

interface in profile D1 beneath 32° N, could be caused by a low temperature anomaly. If we assume a −3.3 Mpa/K gradient of the ringwoodite to perovskite plus magnesiowustite phase transformation (Rg→Pv + mw) near 660 km, the 20 km perturbation of the 660-km interface could be caused by a temperature decrease of 240°C. This low temperature anomaly could indicate the presence of a cold detached oceanic slab either accumulating at the base of the mantle transition zone or in the process of sinking into the lower mantle. If we assume that hot upwelling material has led to the depression of the 410-km interface, the hot material most probably originate from the mantle transition zone but not from the lower mantle, since we observed no significant elevation of the 660-km interface. If we assume the Clapeyron slope of the olivine to wadsleyite ($\alpha\rightarrow\beta$ spinel) phase transition at 410-km is 2.5 MPa/K [*Shearer*, 1991], the 10 km perturbation of the 410-km interface around 93°E, 34°N corresponds to a temperature increase of 130°C. The upwelling may be associated with counter flow caused by the sub-vertical subduction of Indian continental lithosphere beneath central Tibet [*Tilmann et al.*, 2003]. Since we observed no significant elevation of the 410-km interface beneath BNS, the Indian continental crust may not have reached to this depth beneath northern Tibet. Profile D2 shows that the 660-km interface is located consistently at the expected depth, and the 410-km interface is depressed by less than 10 km. Generally, the fluctuation of the mantle transition interfaces in profile D2 is not as significant as D1.

[27] One way to remove potential systematic errors in the upper mantle velocity model is to subtract the 410-km interface depth from the 660-km interface depth in order to derive the mantle transition zone thickness (Figure 8f). Thickening of the transition zone occurs mostly beneath the Lhasa Terrane (270 km thickness beneath 32° N; 93° E), while thinning of the transition zone occurs beneath Qiangtang Terrane (220 km thickness beneath 34° N; 93° E). This observation is consistent with P wave velocity models that show fast anomalies in the mantle transition zone beneath southern Tibet [e.g., *Replumaz et al.*, 2004]. *Li et al.* [2008] observed high-velocity mantle anomalies beneath southern Tibet from 87°E to 92°E, consistent with the mantle transition zone thickness anomaly resolved in our work. This suggests that this anomaly is the result of subducted Indian continental lithosphere. A conceptual model (Figure 9), which includes a high velocity fragmented oceanic slab, subduction of the Indian continental lithosphere beneath central Tibet, and a counter-flow upwelling to the north of the subduction illustrates our interpretation of the upper mantle images.

[28] Two other discontinuities (520-km interface and 720-km interface) in the mantle transition zone may also relate to subduction and associated mantle convection. We can discern generally continuous 520-km and 720-km discontinuities in profile D2, but not in profile D1. In profile D1, the 520-km and 720-km discontinuities are missing above and below the depression of the 660-km discontinuity (south from 33°N), but are quite pronounced below the 410-km depression (north from 33°N, Figure 8a). The 520-km discontinuity is caused by the phase transition from wadsleyite to ringwoodite, the sharpness of which is sensitive to temperature. The transition tends to be sharp in hot mantle and
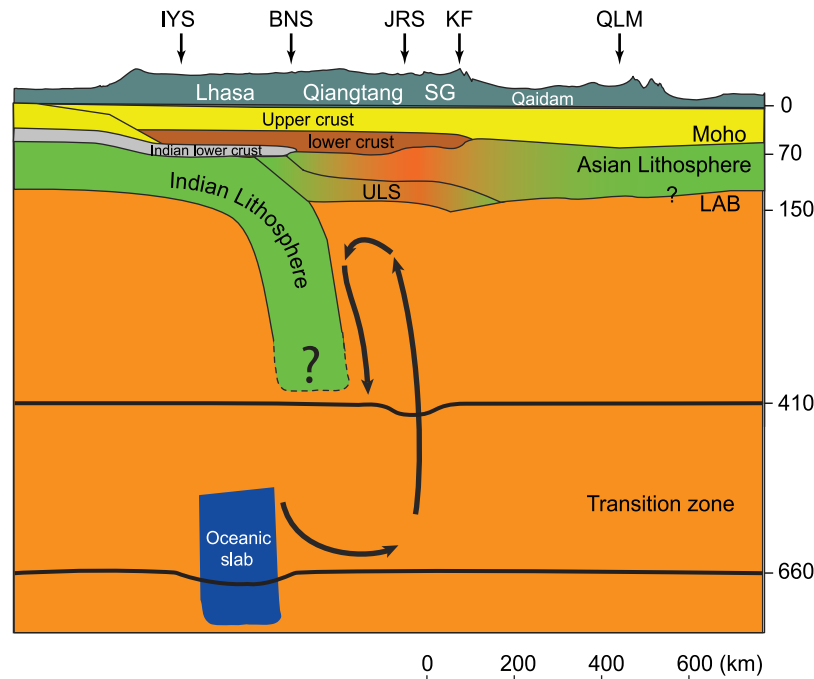
Figure 9. Crust and upper mantle architecture of the central Tibetan Plateau (92°–93° E). The depressed 410-km and 660-km discontinuities can be explained by the Indian oceanic slab sinking to the base of the upper mantle and associated small scale convection extending below the 410-km depth, respectively [*Kosarev et al.*, 1999; *Kind et al.*, 2002; *Tilmann et al.*, 2003; *Li et al.*, 2008]. Underthrusted Lhasa block lithosphere extends from the Bangong-Nujiang suture to the Kunlun Mountains, and now lies dormant beneath the Qiangtang Terrane. The uppermost mantle and the crust is heated by mantle upwelling, which cause a hot, low velocity environment [*Liang and Song*, 2006; *McNamara et al.*, 1995; *Yang et al.*, 2010; *Bao et al.*, 2011; *Wang et al.*, 2012; *Fan et al.*, 2012] in the central Qiangtang and Songpan-Ganzi Terranes.

gradual in cold mantle [*Stixrude*, 1997]. The sharpness variation of the 520-km discontinuity in profile D1 may reflect the temperature contrast between the subducting slab and the upwelling mantle convection. The 720-km discontinuity, associated with the phase transformation from garnet to perovskite, is sensitive to the mantle composition. Since oceanic mantle has much less garnet than the ambient mantle, the mantle beneath the 660-km interface depression, which is mixed with the subducted oceanic mantle, should be depleted in garnet as well. The missing 720-km discontinuity may imply that the lower mantle is mixed with subducted oceanic slab [*Deuss et al.*, 2006]. The missing 720-km discontinuity below the 660-km depression implies that the delaminated oceanic slab may penetrate the 660-km interface and reach at least as deep as 720-km.

[29] Variation of mantle transition zone thickness is limited to west of 94°E beneath the Qiangtang and Songpan-Ganzi Terranes. The upper mantle in this region is characterized by low Pn velocity, high attenuation, and low Rayleigh phase velocity [*McNamara et al.*, 1995; *Liang and Song*, 2006; *Yang et al.*, 2010; *Bao et al.*, 2011; *Wang et al.*, 2012]. The crust beneath this region is also characterized by high Vp/Vs ratio, relatively shallow Moho depth and low shear wave velocity [*Fan et al.*, 2012]. This region has shallow hot springs and normal faulting. These geological characteristics suggest a hot low velocity environment throughout the crust and upper mantle. If we relate this shallow environment to

the return flow produced by subduction, then the subduction and the induced effects are concentrated beneath central Tibet west of 94°E.

4. Conclusion

[30] We have found substantial evidence for a thick Tibetan crust with little Moho topography change except across the major Terrane boundaries and in the foreland fold-thrust-belt (Qaidam Basin and Qilian Mountains). There is a 5–10 km Moho offset beneath the JRS and a ~20 km offset beneath the KF. The Moho interface beneath the Qaidam Basin dips to the north with a dip angle of 5°, which is consistent with loading of the Qilian Mountains on the Qaidam lithosphere and causes the southward shallowing of the sedimentary basin. The crustal Vp/Vs ratio throughout much of northeastern Tibet is close to global average, and does not suggest widespread crustal melting. A higher average Vp/Vs ratio (~1.83) is observed in the crust under the central part of the Qiangtang Terrane and could be the result of the Eocene magmatic event.

[31] Significant lithospheric mantle wave conversion boundaries beneath the Qiangtang and Songpan-Ganzi Terranes in northern Tibet were observed in both the migrated PRF and the stacked SRF images. We interpret these shallow mantle discontinuities as either the base of preserved underthrusted Lhasa lithospheric slab or a remnant oceanic

slab that preceded it. We do not observe any evidence for ongoing continental underthrusting of the Qaidam lithosphere southward beneath the northern Tibetan Plateau.

[32] In the mantle transition zone, we observe a depressed 410-km discontinuity under northern Tibet and a 660-km interface depression under central Tibet. The variation of the mantle transition zone thickness is probably related to sinking of an oceanic plate in the mantle transition zone and associated small-scale convection. Continental subduction and its induced counter flow appear to be limited to central and northern Tibet and do not extend eastward of 94°E. The upwelling counter flow may be responsible for a hot, low seismic velocity environment in the upper mantle and crust under central Qiangtang and Songpan-Ganzi Terranes.

References

Anderson, D. L. (2007), The eclogite engine: Chemical geodynamics as a Galileo Thermometer, *Spec. Pap. Geol. Soc. Am.*, *430*, 47–64, doi:10.1130/2007.2430(03).

Angus, D. A., D. C. Wilson, E. Sandvol, and J. F. Ni (2006), Lithospheric structure of the Arabian and Eurasian collision zone in eastern Turkey from S-wave receiver functions, *Geophys. J. Int.*, *166*(3), 1335–1346, doi:10.1111/j.1365-246X.2006.03070.x.

Argand, E. (1924), La tectonique de l'Asie, *Proc. Int. Geol. Congr.*, *7*, 170–372.

Arndt, N. T., N. Coltice, H. Helmstaedt, and M. Gregoire (2009), Origin of Archean subcontinental lithospheric mantle: Some petrological constraints, *Lithos*, *109*(1–2), 61–71, doi:10.1016/j.lithos.2008.10.019.

Asencio, E., J. H. Knap, T. J. Owens, and G. Helffrich (2003), Mapping fine-scale heterogeneities in the continental mantle lithosphere beneath Scotland: Combining active- and passive-source seismology, *Geology*, *31*(6), 477–480, doi:10.1130/0091-7613(2003)031<0477:MFHWTC>2.0.CO;2.

Bao, X., E. Sandvol, J. Ni, T. Hearn, Y. J. Chen, and Y. Shen (2011), High resolution regional seismic attenuation tomography in eastern Tibetan Plateau and adjacent regions, *Geophys. Res. Lett.*, *38*, L16304, doi:10.1029/2011GL048012.

Bird, P. (1988), Formation of the Rocky Mountains, western United States: A continuum computer model, *Science*, *239*, 1501–1507, doi:10.1126/science.239.4847.1501.

Bostock, M. G. (1998), Mantle stratigraphy and evolution of the Slave province, *J. Geophys. Res.*, *103*(B9), 21,183–21,200, doi:10.1029/98JB01069.

Bostock, M., S. Rondenay, and J. Shragge (2001), Multiparameter two-dimensional inversion of scattered teleseismic body waves: 1. Theory for oblique incidence, *J. Geophys. Res.*, *106*(B12), 30,771–30,782, doi:10.1029/2001JB000330.

Brown, L. D., W. Zhao, K. D. Nelson, M. Hauck, D. Alsdorf, A. Ross, M. Cogan, M. Clark, X. Liu, and J. Che (1996), Bright spots, structure, and magmatism in southern Tibet from INDEPTH seismic reflection profiling, *Science*, *274*(5293), 1688–1690, doi:10.1126/science.274.5293.1688.

Champagnac, J.-D., D.-Y. Yuan, W.-P. Ge, P. Molnar, and W.-J. Zheng (2010), Slip rate at the north-eastern front of the Qilian Shan, China, *Terra Nova*, *22*(3), 180–187, doi:10.1111/j.1365-3121.2010.00932.x.

Chen, L., T. Zheng, and W. Xu, (2006), A thinned lithospheric image of the Tanlu Fault Zone, eastern China: Constructed from wave equation based receiver function migration, *J. Geophys. Res.*, *111*, B09312, doi:10.1029/2005JB003974.

Chen, W.-P., and T.-L. Tseng (2007), Small 660-km seismic discontinuity beneath Tibet implies resting ground for detached lithosphere, *J. Geophys. Res.*, *112*, B05309, doi:10.1029/2006JB004607.

Chen, Z., B. C. Burchfiel, Y. Liu, R. W. King, L. H. Royden, W. Tang, E. Wang, J. Zhao, and X. Zhang (2000), Global Positioning System measurements from eastern Tibet and their implications for India/Eurasia intercontinental deformation, *J. Geophys. Res.*, *105*, 16,215–16,227, doi:10.1029/2000JB900092.

Christensen, N. I. (1996), Poisson's ratio and crustal seismology, *J. Geophys. Res.*, *101*(B2), 3139–3156, doi:10.1029/95JB03446.

Connolly, J. A. D., and D. M. Kerrick (2002), Metamorphic controls on seismic velocity of subducted oceanic crust at 100–250 km depth, *Earth Planet. Sci. Lett.*, *204*(1–2), 61–74, doi:10.1016/S0012-821X(02)00957-3.

Cowgill, E., R. D. Gold, X. Chen, X.-F. Wang, J. R. Arrowsmith, and J. Southon (2009), Low Quaternary slip rate reconciles geodetic and geologic rates along the Altyn Tagh fault northwestern Tibet, *Geology*, *37*(7), 647–650, doi:10.1130/G25623A.1.

Currie, C. A., and C. Beaumont (2011), Are diamond-bearing Cretaceous kimberlites related to low-angle subduction beneath western North America?, *Earth Planet. Sci. Lett.*, *303*(1–2), 59–70, doi:10.1016/j.epsl.2010.12.036.

Dellinger, J. A., S. H. Gray, G. E. Murphy, and J. T. Etgen (2000), Efficient 2.5-D true-amplitude migration, *Geophysics*, *65*(3), 943–950, doi:10.1190/1.1444790.

Deuss, A. (2009), Global observations of mantle discontinuities using SS and PP precursors, *Surv. Geophys.*, *30*(4–5), 301–326, doi:10.1007/s10712-009-9078-y.

Deuss, A., S. A. T. Redfern, K. Chambers, and J. H. Woodhouse (2006), The nature of the 660-kilometer discontinuity in Earth's mantle from global seismic observations of PP precursors, *Science*, *311*(5758), 198–201, doi:10.1126/science.1120020.

Dewey, J. F., and C. A. Burke (1973), Tibetan, Variscan, and Precambrian basement reactivation: Products of continental collision, *J. Geol.*, *81*(6), 683–692, doi:10.1086/627920.

Ding, L., P. Kapp, D. L. Zhong, and W. M. Deng (2003), Cenozoic volcanism in Tibet: Evidence for a transition from oceanic to continental subduction, *J. Petrol.*, *44*(10), 1833–1865, doi:10.1093/petrology/egg061.

Dueker, K., and A. Sheehan (1997), Mantle discontinuity structure from midpoints stacks of converted P and S waves across the Yellowstone hotspot track, *J. Geophys. Res.*, *102*, 8313–8327, doi:10.1029/96JB03857.

England, P., and M. Searle (1986), The Cretaceous-Tertiary deformation of the Lhasa block and its implications for crustal thickening in Tibet, *Tectonics*, *5*(1), 1–14, doi:10.1029/TC005i001p00001.

Fan, W., et al. (2012), Crust and upper mantle velocity structure of the eastern Tibetan Plateau and adjacent regions from ambient noise tomography, *Chin. J. Geophys.*, in press.

Farra, V., and L. Vinnik (2000), Upper mantle stratification by P and S receiver functions, *Geophys. J. Int.*, *141*(3), 699–712, doi:10.1046/j.1365-246x.2000.00118.x.

Fee, D., and K. Dueker (2004), Mantle transition zone topography and structure beneath the Yellowstone hotspot, *Geophys. Res. Lett.*, *31*, L18603, doi:10.1029/2004GL020636.

Gan, W., P. Zhang, Z.-K. Shen, Z. Niu, M. Wang, Y. Wan, D. Zhou, and J. Cheng (2007), Present-day crustal motion within the Tibetan Plateau inferred from GPS measurements, *J. Geophys. Res.*, *112*, B08416, doi:10.1029/2005JB004120.

Girardeau, J., J. Marcoux, C. J. Allègre, J. P. Bassoullet, Y. Tang, X. Xiao, Y. Zao, and X. Wang (1984), Tectonic environment and geodynamic significance of the Neo-Cimmerian Donqiao ophiolite, Bangong-Nujiang suture zone, Tibet, *Nature*, *307*, 27–31, doi:10.1038/307027a0.

Gu, Y., A. Dziewonski, and G. Ekstrom (2003), Simultaneous inversion for mantle shear velocity and topography of transition zone discontinuities, *Geophys. J. Int.*, *154*(2), 559–583, doi:10.1046/j.1365-246X.2003.01967.x.

Gubbins, D., A. Barnicoat, and J. Cann (1994), Seismological constraints on the gabbro-eclogite transition in subducted oceanic crust, *Earth Planet. Sci. Lett.*, *122*(1–2), 89–101, doi:10.1016/0012-821X(94)90053-1.

Guo, Z., M. Wilson, J. Liu, and Q. Mao (2006), Post-collisional, potassic and ultrapotassic magmatism of the northern Tibetan Plateau: Constraints on characteristics of the mantle source, geodynamic setting and uplift mechanisms, *J. Petrol.*, *47*(6), 1177–1220, doi:10.1093/petrology/egl007.

Guynn, J. H., P. Kapp, A. Pullen, M. Heizler, G. Gehrels, and L. Ding (2006), Tibetan basement rocks near Amdo reveal "missing" Mesozoic tectonism along the Bangong suture, central Tibet, *Geology*, *34*(6), 505–508, doi:10.1130/G22453.1.

Hacker, B. R., and G. A. Abers (2004), Subduction Factory 3: An Excel worksheet and macro for calculating the densities, seismic wave speeds, and H2O contents of minerals and rocks at pressure and temperature, *Geochem. Geophys. Geosyst.*, *5*, Q01005, doi:10.1029/2003GC000614.

Hacker, B. R., G. A. Abers, and S. M. Peacock (2003), Subduction factory: 1. Theoretical mineralogy, densities, seismic wave speeds, and H$_2$O contents, *J. Geophys. Res.*, *108*(B1), 2029, doi:10.1029/2001JB001127.

Helffrich, G. (2000), Topography of the transition zone seismic discontinuities, *Rev. Geophys.*, *38*(1), 141–158, doi:10.1029/1999RG000060.

Hirose, K. (2002), Phase transitions in pyrolitic mantle around 670-km depth: Implications for upwelling of plumes from the lower mantle, *J. Geophys. Res.*, *107*(B4), 2078, doi:10.1029/2001JB000597.

Houseman, G., and P. England (1986), Finite strain calculations of continental deformation: 1. Method and general results for convergent zones, *J. Geophys. Res.*, *91*(B3), 3651–3663, doi:10.1029/JB091iB03p03651.

Kapp, P., P. G. DeCelles, G. E. Gehrels, M. Heizler, and L. Ding (2007), Geological records of the Lhasa–Qiangtang and Indo-Asian collisions in the Nima area of central Tibet, *Geol. Soc. Am. Bull.*, *119*(7–8), 917–933, doi:10.1130/B26033.1.

Karplus, M. S., W. Zhao, S. L. Klemperer, Z. Wu, J. Mechie, D. Shi, L. D. Brown, and C. Chen (2011), Injection of Tibetan crust beneath the south Qaidam Basin: Evidence from INDEPTH IV wide-angle seismic data, *J. Geophys. Res.*, *116*, B07301, doi:10.1029/2010JB007911.

Kennett, B. L. N. (1991), The removal of free-surface interactions from 3-component seismograms, *Geophys. J. Int.*, *104*(1), 153–154, doi:10.1111/j.1365-246X.1991.tb02501.x.

Kind, R., et al. (2002), Seismic images of crust and upper mantle beneath Tibet: Evidence for Eurasian plate subduction, *Science*, *298*(5596), 1219–1221, doi:10.1126/science.1078115.

Kosarev, G., R. Kind, S. V. Sobolev, X. Yuan, W. Hanka, and S. Oreshin (1999), Seismic evidence for a detached Indian lithospheric mantle beneath Tibet, *Science*, *283*(5406), 1306–1309, doi:10.1126/science. 283.5406.1306.

Kumar, P., X. H. Yuan, R. Kind, and J. Ni (2006), Imaging the colliding Indian and Asian lithospheric plates beneath Tibet, *J. Geophys. Res.*, *111*, B06308, doi:10.1029/2005JB003930.

Langston, C. A. (1979), Structure under Mount Rainier, Washington, inferred from teleseismic body waves, *J. Geophys. Res.*, *84*(B9), 4749–4762, doi:10.1029/JB084iB09p04749.

Laske, G., G. Masters, and C. Reif (2000), CRUST 2.0: A new global crustal model at 2 × 2 degrees, Inst. of Geophys. and Planet. Phys., Univ. of Calif., San Diego, La Jolla. [Available at http://igppweb.ucsd.edu/~gabi/rem.html]

Lawrence, J., and P. Shearer (2008), Imaging mantle transition zone thickness with SdS-SS finite-frequency sensitivity kernels, *Geophys. J. Int.*, *174*(1), 143–158, doi:10.1111/j.1365-246X.2007.03673.x.

Li, C., R. D. Van der Hilst, A. S. Meltzer, and E. R. Engdahl (2008), Subduction of the Indian lithosphere beneath the Tibetan Plateau and Burma, *Earth Planet. Sci. Lett.*, *274*(1–2), 157–168, doi:10.1016/j.epsl.2008.07.016.

Liang, C. T., and X. D. Song (2006), A low velocity belt beneath northern and eastern Tibetan Plateau from Pn tomography, *Geophys. Res. Lett.*, *33*, L22306, doi:10.1029/2006GL027926.

Ligorria, J., and C. Ammon (1999), Iterative deconvolution and receiver-function estimation, *Bull. Seismol. Soc. Am.*, *89*(5), 1395.

McNamara, D. E., T. J. Owens, and W. R. Walter (1995), Observations of regional phase propagation across the Tibetan Plateau, *J. Geophys. Res.*, *100*(B11), 22,215–22,229, doi:10.1029/95JB01863.

Molnar, P. (1988), A review of geophysical constraints on the deep structure of the Tibetan Plateau, the Himalaya and the Karakoram, and their tectonic implications, *Philos. Trans. R. Soc. London, Ser. A*, *326*(1589), 33–88, doi:10.1098/rsta.1988.0080.

Nábělek, J., G. Hetenyi, J. Vergne, S. Sapkota, B. Kafle, M. Jiang, H. Su, J. Chen, B. S. Huang, and the Hi-CLIMB Team (2009), Underplating in the Himalaya-Tibet collision zone revealed by the Hi-CLIMB experiment, *Science*, *325*, 1371–1374, doi:10.1126/science.1167719.

Nelson, K. D., et al. (1996), Partially molten middle crust beneath southern Tibet: Synthesis of project INDEPTH results, *Science*, *274*(5293), 1684–1688, doi:10.1126/science.274.5293.1684.

Ni, J., and M. Barazangi (1983), Velocities and propagation characteristics of Pn, Pg, Sn, and Lg seismic waves beneath the Indian Shield, Himalayan Arc, Tibetan Plateau, and surrounding regions: High uppermost mantle velocities and efficient Sn propagation beneath Tibet, *Geophys. J. R. Astron. Soc.*, *72*, 665–689, doi:10.1111/j.1365-246X.1983.tb02826.x.

Ni, J., and M. Barazangi (1984), Seismotectonics of the Himalayan collision zone: Geometry of the underthrusting Indian Plate beneath the Himalaya, *J. Geophys. Res.*, *89*(B2), 1147–1163, doi:10.1029/JB089iB02p01147.

Owens, T. J., and G. Zandt (1997), Implications of crustal property variations for models of Tibetan Plateau evolution, *Nature*, *387*(6628), 37–43, doi:10.1038/387037a0.

Owens, T. J., G. E. Randall, F. T. Wu, and R. Zeng (1993), Passcal instrument performance during the Tibetan Plateau Passive Seismic Experiment, *Bull. Seismol. Soc. Am.*, *83*(6), 1959–1970.

Powell, C. M., and P. J. Conaghan (1973), Plate tectonics and the Himalayas, *Earth Planet. Sci. Lett.*, *20*, 1–12, doi:10.1016/0012-821X(73)90134-9.

Replumaz, A., H. Kárason, R. D. van der Hilst, J. Besse, and P. Tapponnier (2004), 4-D evolution of SE Asia's mantle from geological reconstructions and seismic tomography, *Earth Planet. Sci. Lett.*, *221*(1–4), 103–115, doi:10.1016/S0012-821X(04)00070-6.

Ritzwoller, M. H., N. M. Shapiro, M. P. Barmin, and A. L. Levshin (2002), Global surface wave diffraction tomography, *J. Geophys. Res.*, *107*(B12), 2335, doi:10.1029/2002JB001777.

Roger, F., P. Tapponnier, N. Arnaud, U. Schärer, M. Brunel, X. Zhiqin, and Y. Jingsui (2000), An Eocene magmatic belt across central Tibet: Mantle subduction triggered by the Indian collision, *Terra Nova*, *12*(3), 102–108, doi:10.1046/j.1365-3121.2000.123282.x.

Shapiro, N. M., M. H. Ritzwoller, P. Molnar, and V. Levin (2004), Thinning and flow of Tibetan crust constrained by seismic anisotropy, *Science*, *305*(5681), 233–236, doi:10.1126/science.1098276.

Shearer, P. (1991), Constraints on upper mantle discontinuities from observations of long-period reflected and converted phases, *J. Geophys. Res.*, *96*(B11), 18,147–18,182, doi:10.1029/91JB01592.

Shearer, P. M. (2000), Upper mantle seismic discontinuities, in *Earth's Deep Interior: Mineral Physics and Tomography From the Atomic to the Global Scale*, *Geophys. Monogr. Ser.*, vol. 117, edited by S. Karato et al., pp. 115–131, AGU, Washington, D. C., doi:10.1029/GM117p0115.

Shen, Z., M. Wang, W. Gan, and Z. Zhang (2003), Contemporary tectonic strain rate field of Chinese continent and its geodynamic implications, *Earth Sci. Front.*, *10*, suppl., 93–100.

Shi, D. N., Y. Shen, W. J. Zhao, and A. B. Li (2009), Seismic evidence for a Moho offset and south-directed thrust at the easternmost Qaidam-Kunlun boundary in the Northeast Tibetan Plateau, *Earth Planet. Sci. Lett.*, *288*(1–2), 329–334, doi:10.1016/j.epsl.2009.09.036.

Sol, S., et al. (2007), Geodynamics of the southeastern Tibetan Plateau from seismic anisotropy and geodesy, *Geology*, *35*(6), 563–566, doi:10.1130/G23408A.1.

Stixrude, L. (1997), Structure and sharpness of phase transitions and mantle discontinuities, *J. Geophys. Res.*, *102*, 14,835–14,852, doi:10.1029/97JB00550.

Styron, R., M. Taylor, and K. Okoronkwo (2010), Database of active structures from the Indo-Asian collision, *Eos Trans. AGU*, *91*(20), 181, doi:10.1029/2010EO200001.

Tapponnier, P., and P. Molnar (1977), Active faulting and tectonics in China, *J. Geophys. Res.*, *82*(20), 2905–2930, doi:10.1029/JB082i020p02905.

Tapponnier, P., G. Peltzer, A. Y. Ledain, R. Armijo, and P. Cobbold (1982), Propagating extrusion tectonics in Asia: New insights from simple experiments with plasticine, *Geology*, *10*(12), 611–616, doi:10.1130/0091-7613(1982)10<611:PETIAN>2.0.CO;2.

Thomas, C., and M. I. Billen (2009), Mantle transition zone structure along a profile in the SW Pacific: Thermal and compositional variations, *Geophys. J. Int.*, *176*(1), 113–125, doi:10.1111/j.1365-246X.2008.03934.x.

Tilmann, F., J. Ni, and INDEPTH III Team (2003), Seismic imaging of the downwelling Indian lithosphere beneath central Tibet, *Science*, *300*(5624), 1424–1427, doi:10.1126/science.1082777.

Tseng, T.-L., and W.-P. Chen (2008), Discordant contrasts of P- and S-wave speeds across the 660-km discontinuity beneath Tibet: A case for hydrous remnant of sub-continental lithosphere, *Earth Planet. Sci. Lett.*, *268*(3–4), 450–462, doi:10.1016/j.epsl.2008.01.038.

Tseng, T.-L., W.-P. Chen, and R. L. Nowack (2009), Northward thinning of Tibetan crust revealed by virtual seismic profiles, *Geophys. Res. Lett.*, *36*, L24304, doi:10.1029/2009GL040457.

Turcotte, D. L., and G. Schubert (2002), *Geodynamics*, Cambridge Univ. Press, Cambridge, U. K.

Vergne, J., G. Wittlinger, Q. A. Hui, P. Tapponnier, G. Poupinet, J. Mei, G. Herquel, and A. Paul (2002), Seismic evidence for stepwise thickening of the crust across the NE Tibetan Plateau, *Earth Planet. Sci. Lett.*, *203*(1), 25–33, doi:10.1016/S0012-821X(02)00853-1.

Vinnik, L., and V. Farra (2002), Subcratonic low-velocity layer and flood basalts, *Geophys. Res. Lett.*, *29*(4), 1049, doi:10.1029/2001GL014064.

Vlaar, N. J., P. E. van Keken, and A. P. van den Berg (1994), Cooling of the earth in the Archaean: Consequences of pressure-release melting in a hotter mantle, *Earth Planet. Sci. Lett.*, *121*(1–2), 1–18, doi:10.1016/0012-821X(94)90028-0.

Wang, H., et al. (2012), Pn wave tomography of eastern Tibetan Plateau, *Chin. J. Geophys.*, in press.

Washburn, Z., J. R. Arrowsmith, S. L. Forman, E. Cowgill, X. Wang, Y. Zhang, and Z. Chen (2001), Late Holocene earthquake history of the

central Altyn Tagh fault, China, *Geology*, *29*(11), 1051–1054, doi:10.1130/0091-7613(2001)029<1051:LHEHOT>2.0.CO;2.

Weaver, J. S., D. W. Chipman, and T. Takahashi (1979), Comparison between thermochemical and phase stability data for the quartz-coesite-stishovite transformations, *Am. Mineral.*, *64*, 604–614.

Wilson, D., and R. Aster (2003), Imaging crust and upper mantle seismic structure in the southwestern United States using teleseismic receiver functions, *Leading Edge*, *22*(3), 232, doi:10.1190/1.1564528.

Wilson, D. C., D. A. Angus, J. F. Ni, and S. P. Grand (2006), Constraints on the interpretation of S-to-P receiver functions, *Geophys. J. Int.*, *165*(3), 969–980, doi:10.1111/j.1365-246X.2006.02981.x.

Wittlinger, G., F. Masson, G. Poupinet, P. Tapponnier, J. Mei, G. Herquel, J. Guilbert, U. Achauer, X. Guanqi, and S. Danian (1996), Seismic tomography of northern Tibet and Kunlun: Evidence for crustal blocks and mantle velocity contrasts, *Earth Planet. Sci. Lett.*, *139*(1–2), 263–279, doi:10.1016/0012-821X(95)00235-5.

Wittlinger, G., J. Vergne, P. Tapponnier, V. Farra, G. Poupinet, M. Jiang, H. Su, G. Herquel, and A. Paul (2004), Teleseismic imaging of subducting lithosphere and Moho offsets beneath western Tibet, *Earth Planet. Sci. Lett.*, *221*(1–4), 117–130, doi:10.1016/S0012-821X(03)00723-4.

Yang, Y., et al. (2010), Rayleigh wave phase velocity maps of Tibet and the surrounding regions from ambient seismic noise tomography, *Geochem. Geophys. Geosyst.*, *11*, Q08010, doi:10.1029/2010GC003119.

Yin, A., and T. M. Harrison (2000), Geologic evolution of the Himalayan-Tibetan orogen, *Annu. Rev. Earth Planet. Sci.*, *28*(1), 211–280, doi:10.1146/annurev.earth.28.1.211.

Yin, A., et al. (2007), Cenozoic tectonic evolution of Qaidam basin and its surrounding regions (part 2): Wedge tectonics in southern Qaidam basin and the Eastern Kunlun Range, *Spec. Pap. Geol. Soc. Am.*, *433*, 369–390, doi:10.1130/2007.2433(18).

Yin, A., et al. (2008a), Cenozoic tectonic evolution of the Qaidam basin and its surrounding regions (part 3): Structural geology, sedimentation, and regional tectonic reconstruction, *Geol. Soc. Am. Bull.*, *120*(7–8), 847–876, doi:10.1130/B26232.1.

Yin, A., et al. (2008b), Cenozoic tectonic evolution of Qaidam basin and its surrounding regions (part 1): The southern Qilian Shan-Nan Shan thrust belt and northern Qaidam basin, *Geol. Soc. Am. Bull.*, *120*(7–8), 813–846, doi:10.1130/B26180.1.

Yuan, X. H., J. Ni, R. Kind, J. Mechie, and E. Sandvol (1997), Lithospheric and upper mantle structure of southern Tibet from a seismological passive source experiment, *J. Geophys. Res.*, *102*(B12), 27,491–27,500, doi:10.1029/97JB02379.

Yuan, X. H., R. Kind, X. Q. Li, and R. J. Wang (2006), The S receiver functions: Synthetics and data example, *Geophys. J. Int.*, *165*(2), 555–564, doi:10.1111/j.1365-246X.2006.02885.x.

Zheng, D., M. K. Clark, P. Zhang, W. Zheng, and K. A. Farley (2010), Erosion, fault initiation and topographic growth of the North Qilian Shan (northern Tibetan Plateau), *Geosphere*, *6*(6), 937–941, doi:10.1130/GES00523.1.

Zhu, L., and D. V. Helmberger (1998), Moho offset across the northern margin of the Tibetan Plateau, *Science*, *281*(5380), 1170–1172, doi:10.1126/science.281.5380.1170.

Zhu, L., and H. Kanamori (2000), Moho depth variation in southern California from teleseismic receiver functions, *J. Geophys. Res.*, *105*, 2969–2980, doi:10.1029/1999JB900322.